Acta Astronautica 219 (2024) 785–803

Contents lists available at ScienceDirect

Acta Astronautica

journal homepage: www.elsevier.com/locate/actaastro

Research paper

Density-based in-orbit collision risk model valid for any impact geometry

Lorenzo Giudici *, Juan Luis Gonzalo, Camilla Colombo

Department of Aerospace Science and Technology, Politecnico di Milano, Via La Masa 34, 20156, Milan, Italy

ARTICLE INFO

Keywords:
In-orbit collision probability
Space debris cloud
Density propagation
Continuum mechanics

ABSTRACT

Neglecting small fragments in space debris evolutionary models can lead to a significant underestimation of the collision risk for operational satellites. However, when scaling down to the millimetre range, the debris population grows to over a hundred million objects, making deterministic approaches too computationally expensive. On the contrary, probabilistic models provide a more efficient alternative, which however typically works under some simplifying assumptions on the dynamics, limiting their field of applicability. This work proposes an extension of the density-based collision risk models to any orbital dynamics and impact geometry. The impact rate with a target satellite is derived from a multi-dimensional phase space density function in orbital elements, which discretely varies over both phase space and time. The assumption of a bin-wise constant cloud density allows for the analytical transformation of the six-dimensional distribution in orbital elements into the three-dimensional spatial density function, guaranteeing an efficient and accurate evaluation of the fragments flux. The proposed method is applied to the assessment of the collision risk posed by occurred fragmentation events in different orbital regions on a high-risk target object. The effect on the impact rate of the modelling improvements, compared to previous probabilistic formulations, is discussed.

1. Introduction

The number of services provided by in-orbit satellites is massively increasing and, together with that, our exploitation of the space environment. As of today, more than thirty thousand objects are tracked by the space surveillance network, of which only one-third are operational satellites [1]. As motivated in [2], the trackability of space objects strictly depends on the orbital altitude. Due to the current limitations in the sensitivity of radars and telescopes, the lower size threshold for an object to be detected is 1–10 cm in Low-Earth Orbit (LEO), and on the order of 1 m in the Geostationary ring (GEO) [2]. However, excluding smaller fragments when studying the effects of remediation measures for the space debris problem, results in an underestimation of the collision risk for the active satellites population [3]. Experimental data proves that impacts from millimetre-sized particles may compromise the functionality of certain equipment, while centimetre-size projectiles can potentially destroy a satellite in case of a collision [4,5]. Therefore, to have a representative picture of the health and future trend of the space environment, the debris models must have the capability to estimate the actual threat posed to space operations by such small objects. However, when scaling down to the millimetre-size, the population of objects grows to over 100 million [6], representing a barrier even to the computational power of modern computers.

The assessment of the collision risk posed by a population of fragments was historically performed through the Öpik's theory [7]. It provides equations to derive the probability of collision between two objects, based on their orbital elements, under the assumption of zero eccentricity and inclination for one of the two. This assumption was eliminated in a later extension by Wetherill [8]. Kessler extended the model to compute the impact risk from the spatial density of a debris population, assuming an equally probable distribution of the fragments in longitude of the node, argument of periapsis, and mean anomaly, and fixed semi-major axis, eccentricity and inclination [9,10]. Because of the uniform distribution of the particles in longitude, the spatial density was evaluated according to a two-dimensional discretisation of the physical space in altitude and latitude. Such approximation does not allow the applicability of the model to any orbital regime [11]. Indeed, under some initial conditions, randomisation may take long to occur and the fragments orbit shape and orientation may be considerably distorted by orbital perturbations.

Semi-deterministic debris evolutionary models were developed to answer this necessity. Firstly introduced by Rossi et al. [12,13], these methods accomplished the propagation of debris populations under any force model, by gathering the fragments in some representative samples, whose orbit is propagated in time [14–16]. The relative simplicity of the method makes it very flexible to include additional complexities, as predictive launch models or active debris removal. The CUBE algorithm was developed for the accurate evaluation of the

* Corresponding author.
E-mail addresses: lorenzo1.giudici@polimi.it (L. Giudici), juanluis.gonzalo@polimi.it (J.L. Gonzalo), camilla.colombo@polimi.it (C. Colombo).

https://doi.org/10.1016/j.actaastro.2024.03.067
Received 6 November 2023; Received in revised form 15 February 2024; Accepted 31 March 2024
Available online 6 April 2024
0094-5765/© 2024 The Author(s). Published by Elsevier Ltd on behalf of IAA. This is an open access article under the CC BY-NC-ND license (http://creativecommons.org/licenses/by-nc-nd/4.0/).

collision hazard caused by the evolving fragments population [17]. The model divides the physical space into sufficiently small volumes and estimates the spatial density of objects through a uniform sampling of the system in time. Whenever two objects share the same cube, the collision probability is estimated according to their spatial density, their relative velocity, the collision cross-sectional area, and the volume of the cube.

The bottleneck of the semi-deterministic approaches remains the computational cost. For this reason, efficient analytical and semi-analytical probabilistic debris models were also developed. Through an analogy with fluid dynamics, these methods treat the fragments no longer as individual pieces but as a fluid, which continuously deforms under the effect of external disturbances, such as the orbital perturbations. The evolution of the cloud density is retrieved through the time integration of the continuity equation [18–20]. In the work by Letizia et al. [20], the collision probability was evaluated according to the formulation by Kessler [9], but from a one-dimensional time-varying spatial density function dependent on orbital radius. The method assumes the debris cloud as uniformly distributed in a circular band around the Earth and the target object moving on a circular orbit, which constrains its applicability to LEO. Instead, the dependency on the fragments distribution over longitude was included in a dedicated GEO model proposed in [21].

The STARLING suite was developed at Politecnico di Milano with the aim of extending the continuum approach to any orbital regime [22]. The suite numerically integrates the continuity equation through the Method Of Characteristics (MOC) in the phase space of Keplerian elements and area-to-mass ratio, and retrieves the density distribution by fitting a Gaussian Mixture Model (GMM) to the propagated bulk of samples. However, when the third-body perturbation and solar radiation pressure have a predominant effect on the cloud evolution, they may induce bifurcations on a small subset of the phase space, branching out part of the distribution from the main bulk of characteristics. When such condition occurs, the interpolation through the GMM fails [22], limiting the applicability of the model to simplified dynamical regimes. In [23], Frey et al. derived an equation for the estimation of the impact rate between a fragmentation cloud and a target satellite, directly from the six-dimensional phase space density in Keplerian elements. Nevertheless, due to the current limitations of the model, its use was still limited to LEO, assuming fixed fragments inclination and cloud randomisation over longitude of the node and argument of periapsis.

This work aims to extend the density-based collision probability models to any orbital regime. It adopts the continuum propagation method proposed in [24] for the estimation of the debris cloud evolution in time, under the effect of any force model. The resulting evolving density function discretely varies over the phase space of orbital elements, and time. Under this condition, it is demonstrated how the impact rate with a target satellite can be conveniently evaluated through the piece-wise analytical integration of the fragments flux over the target area. This guarantees an efficient and very accurate estimation of the effect of a fragmentation event on the space environment, applicable to any orbital region.

The paper is organised as follows:

- Section 2 gives an overview of the cloud propagator method presented in [24], and adopted as input for the collision risk model within this article.
- Section 3 is the core of this work. Firstly, the collision risk model for LEO fragmentations proposed by Letizia et al. [20] is explained and updated, to stress the similarity with the developed approach. Secondly, the novel and more general collision risk assessment method, valid under any orbital regime, is presented.
- Section 4 is devoted to the application of the theory to occurred fragmentation events. The model is primarily validated against the formulation proposed by Letizia et al. [20], updated as in Section 3, and against the well-known collision risk method proposed by Kessler [10], still assuming randomisation in longitude of the node and argument of periapsis. The additional features, which the proposed method is able to characterise because of the multidimensional description of the cloud dynamics, are successively included once at a time, to evaluate their effect on the estimated collision probability.
- Section 5 recaps the main results and achievements of the work.

2. Fragments cloud modelling and propagation overview

This section provides an overview of the method for the modelling and propagation of a potential cloud of fragments generated by either an in-orbit collision or explosion, which was presented in a past work by the authors [24]. The same model is here adopted as input for the collision risk assessment method proposed in Section 3. The cloud propagator is divided into two main parts, as shown in Fig. 1. Each of them is explained in the following sections.

2.1. Probabilistic characterisation of objects breakup

The method adopts a probabilistic reformulation of the NASA Standard Breakup Model (SBM) [23,24]. From the Probability Density Functions (PDFs) provided in [25], the Cumulative Density Functions (CDFs) are retrieved through integration. The CDFs are used to firstly bound the fragments cloud over the 2D phase space of ejection velocity magnitude and area-to-mass ratio. Such boundaries are successively converted into a domain in Keplerian elements and area-to-mass ratio.

The computed domain is discretised into equally-spaced bins, through an automatised definition of the step-sizes according to the average partial derivatives of the density with respect to the orbital elements, over the Keplerian phase space. The average fragments density value for each bin is obtained from the integral average of the density over the bin volume [24]. Note that the density function in Keplerian elements is computed from the original PDF in ejection velocity and area-to-mass ratio through change of variables [23,26].

2.2. Fragments cloud density propagation

Following the same approach pursued by other authors [18,19,22,27], the fragments density is propagated by applying the MOC [28] to the continuity equation. For a first-order Partial Differential Equation (PDE), like the continuity equation, the MOC discovers curves in the phase space, the characteristic curves, along which a PDE transforms into a system of Ordinary Differential Equations (ODEs). For the problem at hand, the system of ODEs reads as:

$$\begin{cases} \frac{\mathrm{d}\boldsymbol{y}}{\mathrm{d}t} = \boldsymbol{F} \\ \frac{\mathrm{d}n}{\mathrm{d}t} = -n\nabla_{\boldsymbol{y}} \cdot \boldsymbol{F} \end{cases} \tag{1}$$

where $\boldsymbol{y}$ are the phase space variables, t is time, $\boldsymbol{F}$ the force model, and n the fragments density. The characteristics, which are uniformly sampled from the phase space, are propagated semi-analytically, as a consequence of the averaging of the dynamics equations over the fast angular variable. To this purpose, the software PlanODyn [29] is employed. It provides the trace of the Jacobian of the averaged dynamics with respect to the mean elements for atmospheric drag, J_2 perturbation, solar radiation pressure and luni-solar perturbations, which is needed in the density equation of Eq. (1). Note that, to improve the computational efficiency, the software allows for a second averaging procedure, over the disturbing body orbital period. Full detail of the implemented dynamical model can be found in [30].

If propagated to the same epoch, the characteristics form a scattered point cloud in the phase space. Therefore, they must be interpolated to retrieve the density distribution in the whole domain. The interpolation is carried out through binning in the phase space of orbital elements and area-to-mass ratio, at specified time epochs, summing up the

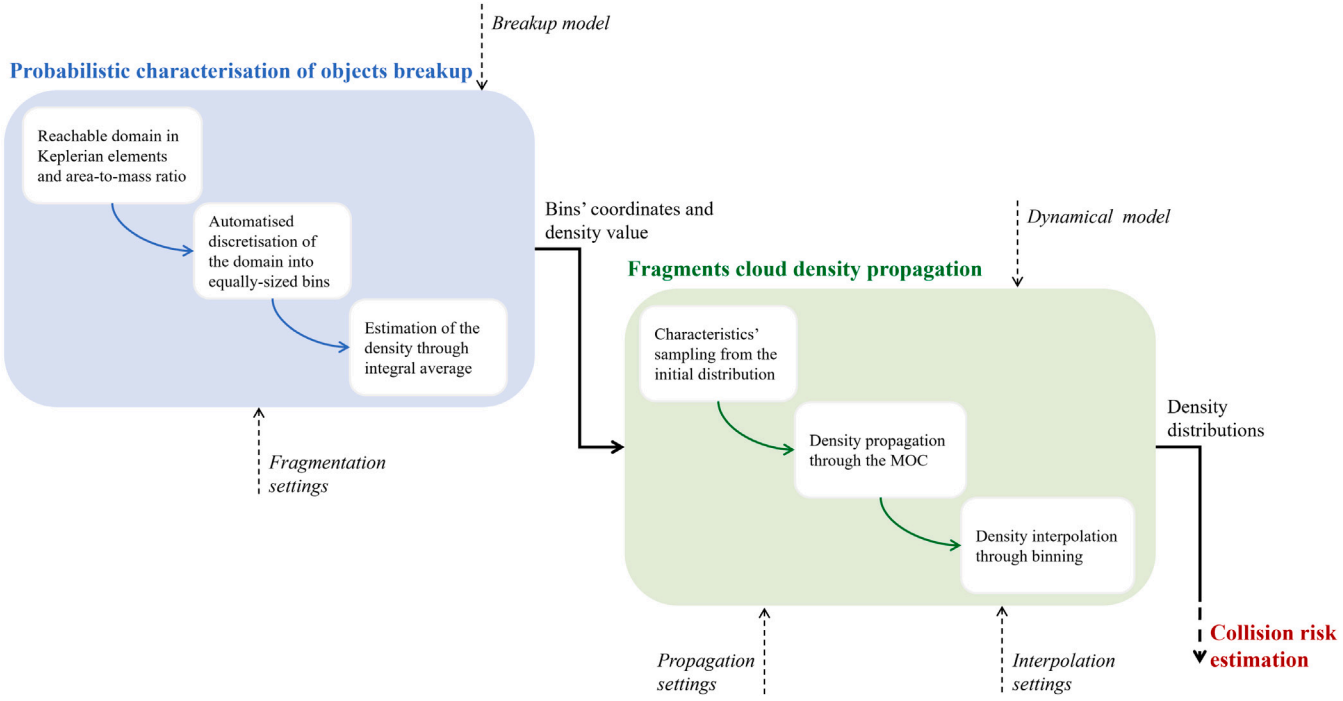

Fig. 1. Block diagram of the debris cloud characterisation and propagation method.

contribution of all the characteristics that share the same volume [24]. As a result, the computed density distribution is bin-wise constant in space and evolves discretely in time. For the results presented in this paper, which focuses on the prediction of the long-term risk posed by breakup events, the fragments mean anomaly is assumed as randomised. In other words, the fragments density n varies as function of the slow-varying orbital elements only, and area-to-mass ratio [24].

3. Fragments density-based collision risk assessment

This section is devoted to explaining the physical and mathematical model developed for the estimation of the probability of collision between a potential fragments cloud, which is described through a phase space density function, and a selected target object.

Firstly, a simplified approach, where the fragments are described through a spatial density function dependent on orbital radius only, is introduced. This method, which was first presented in [20], lacks information on the relative velocity between the target and the fragments, and assumes the latter moving on circular orbits. On the contrary, the cloud propagation model explained in Section 2 allows to estimate the evolution in time of a 6D phase space density function in slow-varying orbital elements and area-to-mass ratio, which ensures the accurate evaluation of the relative velocity of collision. Nevertheless, the simplified collision probability model is presented both to stress the similarity between the two methods and for validation purposes, as detailed in Section 4. Furthermore, some updates are introduced compared to the theory proposed in [20], which allow a better estimate of the impact velocity and the introduction of the non-linear dependency of the spatial density function on latitude in the computation of the collision rate.

The model is then extended to consider the 6D phase space density function. The discrete nature of the density distribution in space and time, resulting from the modelling of the debris cloud through the continuum formulation proposed in Section 2, is exploited to derive a piece-wise analytical expression of the fragments flux over the target cross-sectional area, as a discrete function of time. The knowledge on the impact rate is eventually translated into the cumulative probability of collision with the target, according to a Poisson distribution [31,32]:

$$P_c(t) = 1 - \exp(-\eta(t)) \tag{2}$$

with η cumulative number of collisions over time t. Eq. (2) comes from the common analogy with the gas kinetic theory.

3.1. Impact rate from a 1D spatial density distribution in orbital radius

The average impact rate $\overline{\dot{\eta}}$ between a fragments cloud, described through a 1D spatial density function $n_{\boldsymbol{r}}(r)$, and a target moving on a Keplerian orbit can be approximated as [20]:

$$\overline{\dot{\eta}} = A_c n_{\boldsymbol{r}}(r) \overline{v}_{\text{rel}} \tag{3}$$

with A_c cross-sectional area of the target, and $\overline{v}_{\text{rel}}$ average impact velocity. Letizia et al. [20] pointed out that, for a fragmentation in LEO, the debris cloud forms a band around the Earth in a relatively short period of time. As a result, if the objective is to evaluate the long-term effect of such a cloud, it can be considered randomised over right ascension of the ascending node Ω and argument of periapsis ω. The relative velocity between two objects having a conjunction can be written as function of the velocity moduli and the angle δ between the velocity vectors, as follows.

$$v_{\text{rel}} = \sqrt{v_T^2 + v^2 - 2 v_T v \cos\delta} \tag{4}$$

where v_T and v refer to the velocity moduli of the target and the fragments, respectively. In the remainder of the paper, the subscript $(\cdot)_T$ is used to refer to quantities associated to the target object. The angle δ depends on the target, i_T, and fragments, i, inclination, and the difference in right ascension of the ascending node $\Delta\Omega$ between the two orbits, according to the following relation:

$$\cos\delta = \sin i_T \sin i \cos\Delta\Omega + \cos i_T \cos i \tag{5}$$

Eq. (5) derives from the application of the cosine rule to the green spherical triangle depicted in Fig. 2.

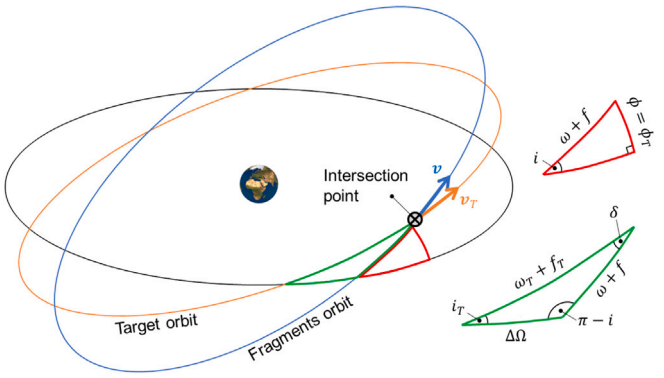

Fig. 2. Spherical triangle of the intersection between the target and fragments orbit.

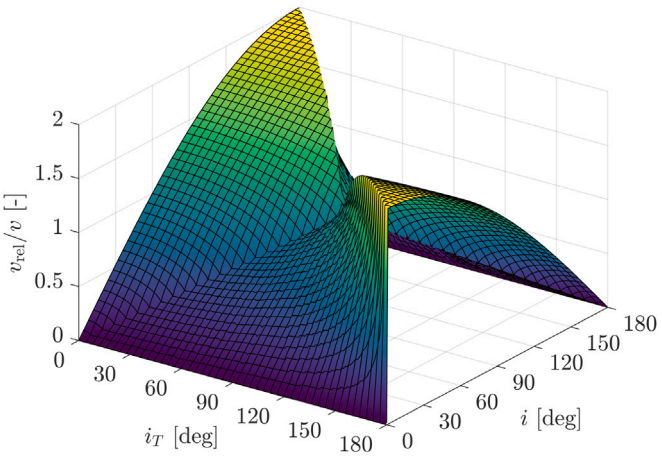

Fig. 3. Impact velocity as function of fragments and target inclination.

In [20], the randomisation over right ascension of the ascending node Ω was misinterpreted as if each $\Delta\Omega$ is equally probable. As a result, the average impact velocity was computed as [20]:

$$\overline{v}_{\text{rel}} = \frac{1}{2\pi}\int_0^{2\pi} v_{\text{rel}}\left(\Delta\Omega\right)\,\mathrm{d}\Delta\Omega \tag{6}$$

However, it must be understood that the average impact velocity $\overline{v}_{\text{rel}}$ corresponds to the mean relative velocity between the fragments and the target, as the latter moves on a fixed Keplerian orbit. Hence, the averaging procedure must be carried out over the mean anomaly M_T of the target, to consider every possible conjunction geometry. For each target mean anomaly M_T, there exist two possible intersecting circular fragments orbits, shifted in right ascension of the ascending node with respect to the target orbit of $\Delta\Omega$, satisfying the cotangent law applied to the green spherical triangle of Fig. 2, i.e.:

$$\cos\Delta\Omega\cos i_T = \cot u_T \sin\Delta\Omega + \cot i \sin i_T \tag{7}$$

where $u_T = \omega_T + f_T$ is the argument of latitude of the target, ω_T and f_T its argument of periapsis and true anomaly, respectively. Thus, the average relative velocity between the target and the fragments can be computed as:

$$\overline{v}_{\text{rel}} = \frac{1}{2\pi}\int_0^{2\pi}\frac{1}{2}\sum_{j=1}^{2} v_{\text{rel}}\left(\Delta\Omega_j\right)\frac{\mathrm{d}M_T}{\mathrm{d}f_T}\,\mathrm{d}f_T \tag{8}$$

with:

$$\frac{\mathrm{d}M_T}{\mathrm{d}f_T} = \frac{\left(1-e_T^2\right)^{3/2}}{\left(1+e_T\cos f_T\right)^2} \tag{9}$$

where e_T is the eccentricity of the target object. Note that $\Delta\Omega_j$ of Eq. (8) indicates one of the two possible solutions of Eq. (7). Fig. 3 shows the average velocity of impact $\overline{v}_{\text{rel}}$, normalised by the velocity on a circular orbit at the altitude of the target, as function of fragments, i, and target, i_T, inclination, assuming they move on circular orbits.

As it can be observed, the surface of solutions is symmetric about the point $(i, i_T) = (90, 90)$ deg. The impact velocity is larger when the fragments move on a prograde orbit with the target object on a retrograde one, or viceversa. In particular, when fragments and target object lie on the equatorial plane, but are characterised by opposite direction of rotation, the normalised average impact velocity is double the orbital velocity v_T. When, instead, they both have zero inclination, under the assumption of circular orbits, the relative velocity nullifies.

Finally, it is worth stressing that Eq. (3) applies only if the target is also moving on a circular orbit. Indeed, the spatial density n_r is assumed to be constant for each target position along its orbit. If, however, the target orbit is elliptical, the orbital radius varies as function of the target mean anomaly M_T. As a result, the spatial density must be included in the integration over M_T, as follows.

$$\overline{\dot{\eta}} = \frac{A_c}{2\pi}\int_0^{2\pi} n_r\left(r_T\right) v^*_{\text{rel}}\left(\Delta\Omega\right)\,\mathrm{d}M_T \tag{10}$$

where v^*_{rel} indicates the mean between the two possible impact velocities, given the target mean anomaly M_T.

A further limitation of the model proposed in [20] is that the spatial density function is assumed to be randomised over both longitude λ and latitude ϕ. However, as motivated in [9], even if the fragments are assumed to share the same orbital inclination, and to be uniformly distributed in a band around the Earth, the spatial density function has a non-linear dependency on latitude ϕ. Indeed, the spatial density in a band with infinitesimal thickness in radial distance $\mathrm{d}r$ and angular amplitude $\mathrm{d}\phi$, as function of orbital radius r and latitude ϕ, can be computed as:

$$n_r(r,\phi) = \frac{\mathrm{d}N(r,\phi)}{\mathrm{d}A(r,\phi)\mathrm{d}r} \tag{11}$$

where N is the number of fragments and A is the surface area of the band around the Earth. The infinitesimal number of fragments can be computed according to the following equation:

$$\mathrm{d}N(r,\phi) = N(r)\frac{\mathrm{d}M}{\pi} = \frac{N(r)}{\pi}\frac{\mathrm{d}M}{\mathrm{d}f}\frac{\mathrm{d}f}{\mathrm{d}\phi}\mathrm{d}\phi \tag{12}$$

Assuming the fragments orbit as circular for simplicity, Eq. (12) simplifies as follows.

$$\begin{aligned} dN(r,\phi) &= \frac{N(r)}{\pi}\frac{\mathrm{d}f}{\mathrm{d}\phi}\,\mathrm{d}\phi \\ &= \frac{N(r)}{\pi}\frac{\cos\phi}{\sqrt{\sin^2 i - \sin^2\phi}}\,\mathrm{d}\phi \end{aligned} \tag{13}$$

Instead, the infinitesimal area $\mathrm{d}A$ takes the following form:

$$dA(r,\phi) = 2\pi r^2\cos\phi\,\mathrm{d}\phi \tag{14}$$

Therefore, the 2D spatial density function of Eq. (11) modifies as follows.

$$\begin{aligned} n_r(r,\phi) &= \frac{N(r)}{2\pi r^2\mathrm{d}r}\frac{1}{\pi\sqrt{\sin^2 i - \sin^2\phi}} \\ &= n_r(r)\frac{2}{\pi\sqrt{\sin^2 i - \sin^2\phi}} \\ &= n_r(r)\beta(\phi) \end{aligned} \tag{15}$$

which coincides with the expression found by Kessler [9]. As it can be noted, the non-linear dependency of the spatial density function on latitude is introduced by both the true anomaly-latitude relation of Eq. (13) and the dependency of the area of the circular band on latitude, expressed by Eq. (14). In Fig. 4 the latitude-dependent parts of Eq. (13), Eq. (14) and (15) are shown as function of the argument of latitude u, for different values of inclination i. Note that latitude ϕ and argument

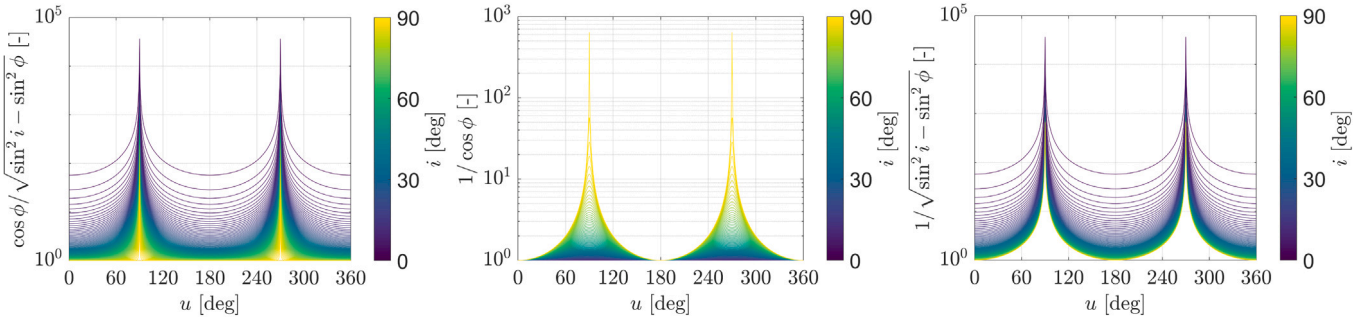

(a) Effect of true anomaly-latitude relation (b) Effect of circular band-latitude relation (c) Combined effect

Fig. 4. Dependency of the spatial density function on latitude.

of latitude u are linked by the sine rule applied to the red spherical triangle of Fig. 2, which provides the following expression:

$$\sin\phi = \sin u \sin i \tag{16}$$

Replacing the 1D spatial density function in Eq. (3) with the 2D density function of Eq. (15), evaluated at the target orbital radius r_T and latitude ϕ_T, allows a more accurate estimation of the impact rate, which accounts for the fragments distribution over latitude. The resulting expression is here reported for completeness:

$$\bar{\dot{\eta}} = \frac{A_c}{2\pi}\int_0^{2\pi} n_{\boldsymbol{r}}\left(r_T\right)\beta\left(\phi_T\right)v_{\mathrm{rel}}^{*}\left(\Delta\Omega\right)\mathrm{d}M_T \tag{17}$$

3.2. Impact rate from a 6D density distribution in orbital elements

Defined as $\gamma := (a, e, i, \Omega, \omega)$ the slow-varying Keplerian elements, with a semi-major axis, e eccentricity, i inclination, Ω right ascension of the ascending node, and ω argument of periapsis, the average impact rate $\bar{\dot{\eta}}$ with a target object with elements $\boldsymbol{\gamma}_T$ takes the general form:

$$\bar{\dot{\eta}} = \frac{1}{2\pi}\int_0^{2\pi} \dot{\eta}\left(\boldsymbol{\gamma}_T, M_T\right)\mathrm{d}M_T \tag{18}$$

If the fragments distribution is represented through a 6D density function in Cartesian coordinates $(\boldsymbol{r}, \boldsymbol{v})$, $n_{\boldsymbol{r},\boldsymbol{v}}$, the impact rate associated to a fixed value of mean anomaly M_T can be approximated as [23]:

$$\dot{\eta}\left(\boldsymbol{\gamma}_T, M_T\right) = A_c \iiint_{\mathbb{R}^3} n_{\boldsymbol{r},\boldsymbol{v}}(\boldsymbol{r}_T, \boldsymbol{v}) v_{\mathrm{rel}}\,\mathrm{d}\boldsymbol{v} \tag{19}$$

where $\boldsymbol{r}$ and $\boldsymbol{v}$ indicate the position and velocity vectors of the fragments. The main assumption behind Eq. (19) is that the fragments cross-sectional areas are assumed to be negligible if compared to the target one. As demonstrated in [23], the 6D density function in Cartesian coordinates, evaluated at the target position $\boldsymbol{r}_T$, can be related to the phase space density in Keplerian elements, $n_{\boldsymbol{\alpha},\boldsymbol{\beta}}$, with $\boldsymbol{\alpha} := (a, e, i)$ and $\boldsymbol{\beta} := (\Omega, \omega, M)$, according to the following equation:

$$n_{\boldsymbol{r},\boldsymbol{v}}(\boldsymbol{r}_T, \boldsymbol{v})\,\mathrm{d}\boldsymbol{v} = \sum_{k=1}^{4} \frac{n_{\boldsymbol{\alpha},\boldsymbol{\beta}}\left(\boldsymbol{\alpha}, \boldsymbol{\beta}^{(k)}\right)}{\left|\det \boldsymbol{J}_{\boldsymbol{r}\to\boldsymbol{\beta}}^{(k)}\right|}\,\mathrm{d}\boldsymbol{\alpha} \tag{20}$$

where $\boldsymbol{J}_{\boldsymbol{r}\to\boldsymbol{\beta}}$ is the Jacobian of the transformation from position vector $\boldsymbol{r}$ to the subset of the Keplerian elements (Ω, ω, M), i.e.:

$$\boldsymbol{J}_{\boldsymbol{r}\to\boldsymbol{\beta}} = \begin{bmatrix} \frac{\partial r_x}{\partial\Omega} & \frac{\partial r_x}{\partial\omega} & \frac{\partial r_x}{\partial M} \\ \frac{\partial r_y}{\partial\Omega} & \frac{\partial r_y}{\partial\omega} & \frac{\partial r_y}{\partial M} \\ \frac{\partial r_z}{\partial\Omega} & \frac{\partial r_z}{\partial\omega} & \frac{\partial r_z}{\partial M} \end{bmatrix} \tag{21}$$

whose elements expression can be found in [33]. The absolute value of the determinant of $\boldsymbol{J}_{\boldsymbol{r}\to\boldsymbol{\beta}}$ takes the form:

$$\left|\det \boldsymbol{J}_{\boldsymbol{r}\to\boldsymbol{\beta}}^{(k)}\right| = \frac{a^3 e(1-e^2)^{3/2}\left|\cos\left(\omega^{(k)} + f^{(k)}\right)\sin f^{(k)}\right|\sin i}{(1 + e\cos f^{(k)})^2} \tag{22}$$

The summation in Eq. (20) represents the four possible intersections between the target and fragments orbit, once the target position vector $\boldsymbol{r}_T$ is fixed and the subset of the Keplerian elements $\boldsymbol{\alpha}$ is given. The intersecting orbits are provided by the four combinations $(\boldsymbol{\alpha}, \boldsymbol{\beta}^{(k)})$. In particular, the two solutions of the orbital radius equation:

$$r_T = \frac{a(1-e^2)}{1 + e\cos f} \tag{23}$$

provide the two angular positions f_1 and f_2. The cotangent rule applied to the green spherical triangle of Fig. 2, which is given in Eq. (7), allows the computation of the fragments orbital plane, through the solutions in right ascension of the ascending node Ω_1 and Ω_2. Finally, the application of the sine rule to the same spherical triangle, which states:

$$\sin u_T \sin i_T = \sin u \sin i \tag{24}$$

fixes the fragments orbit in-plane orientation, provided by the solutions in argument of latitude u_1 and u_2. The resulting solutions $\boldsymbol{\beta}^{(k)}$ have the following characteristics:

$$\begin{aligned} \boldsymbol{\beta}^{(1)} &= (\Omega_1, \omega_1, M_1) \\ \boldsymbol{\beta}^{(2)} &= (\Omega_1, \omega_2, M_2) \\ \boldsymbol{\beta}^{(3)} &= (\Omega_2, \omega_3, M_1) \\ \boldsymbol{\beta}^{(4)} &= (\Omega_2, \omega_4, M_2) \end{aligned} \tag{25}$$

and satisfy:

$$\begin{aligned} \omega_1 + f_1(M_1) &= \omega_2 + f_2(M_2) = u_1 \\ \omega_3 + f_1(M_1) &= \omega_4 + f_2(M_2) = u_2 \\ f_1(M_1) &= -f_2(M_2) \end{aligned} \tag{26}$$

Plugging Eqs. (23) and (24) into Eq. (22), the determinant of the Jacobian modifies as:

$$\begin{aligned} \left|\det \boldsymbol{J}_{\boldsymbol{r}\to\boldsymbol{\beta}}^{(k)}\right| &= r_T^2 \frac{ae\sqrt{1-g^2}}{\sqrt{1-e^2}}\sqrt{1-h^2}\sin i \\ &= \frac{1}{\Psi(\boldsymbol{\alpha})} \end{aligned} \tag{27}$$

where the functions $g := g(a, e, r_T)$ and $h := h(i, i_T, \omega_T, f_T)$ are the cosine of the true anomaly f and the sine of the argument of latitude $u = \omega + f$, derived from Eqs. (23) and (24), and the function Ψ, which stands for the absolute value of the inverse of the determinant of $\boldsymbol{J}_{\boldsymbol{r}\to\boldsymbol{\beta}}$, is introduced to simplify the notation. As it can be noticed, the function Ψ is independent of the value of the dependent Keplerian elements Ω, ω, M; thus, it can be taken outside of the summation of Eq. (20).

Plugging Eq. (20) into Eq. (19) allows retrieving the impact rate directly from the phase space density in Keplerian elements, $n_{\boldsymbol{\alpha},\boldsymbol{\beta}}$. In addition, the use of a binning approach for the computation of the phase space density distribution, from the propagated bulk of characteristics, implies that the fragments density varies discretely over the phase space. As a result, the integration over the domain in the

independent Keplerian elements $\boldsymbol{\alpha}$ can be split into a summation of integrals over the bins volume, over which the fragments density is constant. Therefore, the impact rate is approximated as follows.

$$\dot{\eta}(\boldsymbol{\gamma}_T, M_T) = A_c \sum_{j=1}^{N_b^*} \left[\iiint_{V_{\boldsymbol{\alpha}}^{(j)}} \Psi(\boldsymbol{\alpha}) \sum_{k=1}^{4} n_{\boldsymbol{\alpha},\boldsymbol{\beta}}^{(jk)} v_{\mathrm{rel}}^{(k)}(\boldsymbol{\alpha}) \, \mathrm{d}\boldsymbol{\alpha} \right] \tag{28}$$

where $n_{\boldsymbol{\alpha},\boldsymbol{\beta}}^{(jk)}$ is the phase space density in the bin with centre coordinates $\left[\boldsymbol{\alpha}^{(j)}, \boldsymbol{\beta}^{(k)}(\boldsymbol{\alpha}^{(j)})\right]$, $v_{\mathrm{rel}}^{(k)}(\boldsymbol{\alpha})$ is the relative velocity between fragments and target for the kth solution of intersection, given $\boldsymbol{\alpha}$, and N_b^* is the number of bins, whose subset of Keplerian elements (a, e, i) satisfies Eq. (23), Eq. (7) and (24) for some combinations of (Ω, ω, M). Therefore, by adopting a binning approach, the estimation of the impact rate reduces to the computation of the integral of Eq. (28), at bin level, and to the summation of the contribution of each bin ensuring intersection with the target, and having a non-null density value.

The integral of Eq. (28) cannot be solved in closed form. Nevertheless, if the discretisation in (a, e, i) is sufficiently refined, the impact rate can be reduced to:

$$\dot{\eta}(\boldsymbol{\gamma}_T, M_T) = A_c \sum_{j=1}^{N_b^*} \left[\sum_{k=1}^{4} \left(n_{\boldsymbol{\alpha},\boldsymbol{\beta}}^{(jk)} v_{\mathrm{rel}}^{(jk)} \right) \iiint_{V_{\boldsymbol{\alpha}}^{(j)}} \Psi(\boldsymbol{\alpha}) \, \mathrm{d}\boldsymbol{\alpha} \right] \tag{29}$$

with:

$$v_{\mathrm{rel}}^{(jk)} = \left\| \boldsymbol{v}\left(\boldsymbol{\alpha}^{(j)}, \boldsymbol{\beta}^{(k)}(\boldsymbol{\alpha}^{(j)})\right) - \boldsymbol{v}_T \right\| \tag{30}$$

which consists in approximating the relative velocity between the target object and the fragments $v_{\mathrm{rel}}^{(k)}(\boldsymbol{\alpha})$ as the relative velocity in correspondence of the bins centre $v_{\mathrm{rel}}^{(jk)}$, over each bin volume. Note that, the assumption of Eq. (29) means that the spatial density function in correspondence of the target, $n_{\boldsymbol{r}}(\boldsymbol{r}_T)$, is computed without any approximation, net of the mathematical modelling of the phase space density $n_{\boldsymbol{\alpha},\boldsymbol{\beta}}$, while the relative velocity is measured discretely, in correspondence of the bins centre. Indeed, the spatial density $n_{\boldsymbol{r}}(\boldsymbol{r}_T)$ can be obtained from Eq. (20) through integration as follows.

$$\begin{aligned} n_{\boldsymbol{r}}(\boldsymbol{r}_T) &= \iiint_{\mathbb{R}^3} n_{\boldsymbol{r},\boldsymbol{v}}(\boldsymbol{r}_T, \boldsymbol{v}) \, \mathrm{d}\boldsymbol{v} \\ &= \sum_{j=1}^{N_b^*} \left[\sum_{k=1}^{4} \left(n_{\boldsymbol{\alpha},\boldsymbol{\beta}}^{(jk)} \right) \iiint_{V_{\boldsymbol{\alpha}}^{(j)}} \Psi(\boldsymbol{\alpha}) \, \mathrm{d}\boldsymbol{\alpha} \right] \end{aligned} \tag{31}$$

In the following sections the assumption of Eq. (29) is justified, estimating the error introduced by approximating the relative velocity between fragments and target object as bin-wise constant. Two analytical solutions of the integral of the function $\Psi(\boldsymbol{\alpha})$ are then proposed.

3.2.1. Effect of the modelling assumptions on accuracy

To justify the assumption of constant relative velocity over the bins volume, the Taylor expansion of v_{rel} around the bin centre is considered:

$$v_{\mathrm{rel}}^{(k)}(\boldsymbol{\alpha}) = v_{\mathrm{rel}}^{(jk)} + \boldsymbol{J}_{v_{\mathrm{rel}}}^{(jk)} \Delta\boldsymbol{\alpha} + \frac{1}{2} \Delta\boldsymbol{\alpha}^T \boldsymbol{H}_{v_{\mathrm{rel}}}^{(jk)} \Delta\boldsymbol{\alpha} + \dots \tag{32}$$

$$\Delta\boldsymbol{\alpha} = \boldsymbol{\alpha} - \boldsymbol{\alpha}^{(j)}$$

where $\boldsymbol{J}_{v_{\mathrm{rel}}}^{(jk)}$ and $\boldsymbol{H}_{v_{\mathrm{rel}}}^{(jk)}$ are the Jacobian and the Hessian of the impact velocity function $v_{\mathrm{rel}}^{(k)}(\boldsymbol{\alpha})$, evaluated in the bins centre. From now on the apexes, indicating the jth bin and the k$^{\mathrm{th}}$ solution of intersection, are omitted for the sake of simplicity. The Jacobian $\boldsymbol{J}_{v_{\mathrm{rel}}}$ and Hessian $\boldsymbol{H}_{v_{\mathrm{rel}}}$ take the following form:

$$\boldsymbol{J}_{v_{\mathrm{rel}}} = \frac{\boldsymbol{v}_{\mathrm{rel}}^T}{v_{\mathrm{rel}}} \boldsymbol{J}_{\boldsymbol{v}} \tag{33}$$

$$\boldsymbol{H}_{v_{\mathrm{rel}}} = \frac{\boldsymbol{J}_{\boldsymbol{v}}^T \boldsymbol{J}_{\boldsymbol{v}}}{v_{\mathrm{rel}}} - \frac{\boldsymbol{J}_{\boldsymbol{v}}^T \boldsymbol{v}_{\mathrm{rel}} \boldsymbol{v}_{\mathrm{rel}}^T \boldsymbol{J}_{\boldsymbol{v}}}{v_{\mathrm{rel}}^3} + \frac{\boldsymbol{v}_{\mathrm{rel}}^T}{v_{\mathrm{rel}}} \boldsymbol{H}_{\boldsymbol{v}} \tag{34}$$

where $\boldsymbol{J}_{\boldsymbol{v}}$ and $\boldsymbol{H}_{\boldsymbol{v}}$ are Jacobian and Hessian of the fragments velocity vector function $\boldsymbol{v}(\boldsymbol{\alpha})$. Assuming that the step-sizes with which the density distribution is discretised are small enough, the velocity difference between the bin centre and any point in the bin, $\Delta\boldsymbol{v}(\boldsymbol{\alpha})$, can be written from the second order expansion of $\boldsymbol{v}(\boldsymbol{\alpha})$ around the bin centre $\boldsymbol{\alpha}^{(j)}$, as follows.

$$\boldsymbol{v}(\boldsymbol{\alpha}) - \boldsymbol{v} = \Delta\boldsymbol{v}(\boldsymbol{\alpha}) \approx \boldsymbol{J}_{\boldsymbol{v}} \Delta\boldsymbol{\alpha} + \frac{1}{2} \Delta\boldsymbol{\alpha}^T \boldsymbol{H}_{\boldsymbol{v}} \Delta\boldsymbol{\alpha} \tag{35}$$

Introducing Eqs. (33) and (34) into Eq. (32), it is possible to write:

$$\begin{aligned} v_{\mathrm{rel}}(\boldsymbol{\alpha}) \approx\ & v_{\mathrm{rel}} + \frac{\boldsymbol{v}_{\mathrm{rel}}^T}{v_{\mathrm{rel}}} \left(\boldsymbol{J}_{\boldsymbol{v}} \Delta\boldsymbol{\alpha} + \frac{1}{2} \Delta\boldsymbol{\alpha}^T \boldsymbol{H}_{\boldsymbol{v}} \Delta\boldsymbol{\alpha} \right) \\ & + \frac{1}{2} \Delta\boldsymbol{\alpha}^T \left(\frac{\boldsymbol{J}_{\boldsymbol{v}}^T \boldsymbol{J}_{\boldsymbol{v}}}{v_{\mathrm{rel}}} - \frac{\boldsymbol{J}_{\boldsymbol{v}}^T \boldsymbol{v}_{\mathrm{rel}} \boldsymbol{v}_{\mathrm{rel}}^T \boldsymbol{J}_{\boldsymbol{v}}}{v_{\mathrm{rel}}^3} \right) \Delta\boldsymbol{\alpha} \end{aligned} \tag{36}$$

The first bracket is identified as $\Delta\boldsymbol{v} = \Delta\boldsymbol{v}(\boldsymbol{\alpha})$ from Eq. (35). For the last term, because it is already quadratic in $\Delta\boldsymbol{\alpha}$, the expansion in $\boldsymbol{v}(\boldsymbol{\alpha})$ is truncated at the first order, i.e., the linear relation $\Delta\boldsymbol{v} = \boldsymbol{J}_{\boldsymbol{v}} \Delta\boldsymbol{\alpha}$ is used to reach:

$$v_{\mathrm{rel}}(\boldsymbol{\alpha}) \approx v_{\mathrm{rel}} + \frac{\boldsymbol{v}_{\mathrm{rel}}^T \Delta\boldsymbol{v}}{v_{\mathrm{rel}}} + \frac{1}{2} \frac{\Delta\boldsymbol{v}^T \Delta\boldsymbol{v}}{v_{\mathrm{rel}}} - \frac{1}{2} \frac{\Delta\boldsymbol{v}^T \boldsymbol{v}_{\mathrm{rel}} \boldsymbol{v}_{\mathrm{rel}}^T \Delta\boldsymbol{v}}{v_{\mathrm{rel}}^3} \tag{37}$$

Identified as $\rho = \rho(\boldsymbol{\alpha})$ the angle between the vectors $\boldsymbol{v}_{\mathrm{rel}}$ and $\Delta\boldsymbol{v}(\boldsymbol{\alpha})$, Eq. (37) can be rewritten as:

$$v_{\mathrm{rel}}(\boldsymbol{\alpha}) \approx v_{\mathrm{rel}} + \Delta v \cos\rho + \frac{1}{2} \frac{\Delta v^2}{v_{\mathrm{rel}}} \sin^2\rho \tag{38}$$

Thus, the normalised error introduced by the approximation of Eq. (29) can be expressed as follows.

$$\begin{aligned} \mathrm{Err.}(\boldsymbol{\alpha}) &= \frac{v_{\mathrm{rel}}(\boldsymbol{\alpha}) - v_{\mathrm{rel}}}{v_{\mathrm{rel}}} \\ &\approx \xi \cos\rho + \frac{1}{2} \xi^2 \sin^2\rho \end{aligned} \tag{39}$$

with:

$$\xi(\boldsymbol{\alpha}) = \frac{\Delta v(\boldsymbol{\alpha})}{v_{\mathrm{rel}}} \tag{40}$$

Since the step-sizes are taken sufficiently small, the impact velocity v_{rel} is either greater or comparable to the difference in velocity between the bin centre and any point belonging to the bin $\Delta v(\boldsymbol{\alpha})$, for every bin in the domain, or, equivalently:

$$\xi(\boldsymbol{\alpha}) \lesssim 1 \tag{41}$$

However, it is worth recalling that the function $\xi(\boldsymbol{\alpha})$ may approach unity only in those bins (if any) where the relative velocity between the target and the fragments is close to zero, i.e., when they move on very similar orbits in both shape and orientation. On the contrary, for any fragmentation scenario there exist many bins for which $\xi(\boldsymbol{\alpha}) \ll 1$, as the fragments spread out in a considerably vast domain. Therefore, considering that the impact rate is proportional to the impact velocity, the error expressed in Eq. (39) is high only for those bins which provide a negligible contribution to the overall estimated impact rate. Finally, note that if $\xi(\boldsymbol{\alpha})$ is smaller than unity, the following inequality for the error applies:

$$\mathrm{Err.}(\boldsymbol{\alpha}) < \xi(\boldsymbol{\alpha}) \tag{42}$$

This implies that the assumption of Eq. (29) only slightly affects the accuracy of the method.

3.2.2. Semi-analytical computation of the impact rate

The function $\Psi(\boldsymbol{\alpha})$, reported in Eq. (27), can be written as the product among a constant, r_T^3, a function of semi-major axis and eccentricity, $\tilde{g}(a, e)$, and a function of inclination, $\tilde{h}(i)$, whose expressions are:

$$\begin{aligned} \tilde{g}(a, e) &= \frac{1}{a\sqrt{2ar_T - a^2(1 - e^2) - r_T^2}} \\ \tilde{h}(i) &= \frac{1}{\sqrt{\sin^2 i - \sin^2 \phi_T}} \end{aligned} \tag{43}$$

where ϕ_T is the target latitude. As a result, the integrals in semi-major axis and eccentricity, $\mathcal{I}_{a/e}$, and inclination, $\mathcal{I}_i$, can be computed separately. The integration in inclination is firstly addressed.

The primitive $\mathcal{H}(i)$ of the function $\tilde{h}(i)$ reads as:

$$\mathcal{H}(i) = \int \tilde{h}(i)\,\mathrm{d}i = \frac{1j}{\sin\phi_T} F(i,m) \tag{44}$$

$$m = \frac{1}{\sin^2\phi_T}$$

where $1j$ is the imaginary unit, and $F(i,m)$ is the incomplete elliptic integral of the first kind with modulus $m \geq 1\ \forall\phi_T$, whose value is in general complex, unless m is unity. By applying the reciprocal modulus transformation by Byrd and Friedman [34], the elliptic integral $F(i,m)$ can be written as sum of two elliptic integrals for which the solution is always real, as follows.

$$F(i,m) = \sin\phi_T \left[K\left(\frac{1}{m}\right) - 1j\, F\left(\zeta(i), 1 - \frac{1}{m}\right)\right] \tag{45}$$

with:

$$\zeta(i) = \arcsin\left(\frac{\sqrt{m\sin^2 i - 1}}{\sin i\sqrt{m-1}}\right) \tag{46}$$

where $K\left(\frac{1}{m}\right)$ is the complete elliptic integral of the first kind. The evaluation the primitive $\mathcal{H}(i)$ between the two extremes of integration, i_1 and i_2, provides the following expression for the integral in inclination $\mathcal{I}_i$:

$$\mathcal{I}_i = F\left[\zeta(i_2), 1 - \sin^2\phi_T\right] - F\left[\zeta(i_1), 1 - \sin^2\phi_T\right] \tag{47}$$

As it can be observed, the imaginary part cancels out, as it multiplies the complete elliptic integral $K\left(\frac{1}{m}\right)$, which does not depend on inclination by definition. Note also that the primitive $\mathcal{H}(i)$ has a singularity when the following inequality applies:

$$\sin i < |\sin\phi_T| \tag{48}$$

This condition is a physical singularity, as when Eq. (48) is satisfied, the fragments orbit cannot intersect the target one, for any combination of (Ω, ω, M). Indeed, the maximum latitude magnitude reachable by the fragments coincides with their orbital inclination. In general, the two extremes of integration in inclination, i_1 and i_2, can be obtained as follows.

$$\begin{cases} i_1 = \arcsin\left[\max(\sin i^-, |\sin\phi_T|)\right] \\ i_2 = \pi - \arcsin\left[\max(\sin i^+, |\sin\phi_T|)\right] \end{cases} \tag{49}$$

where i^- and i^+ indicate the lower and upper inclination boundaries for the considered bin.

The integral in semi-major axis and eccentricity $\mathcal{I}_{a/e}$ is now considered. The primitive $\mathcal{G}(a,e)$ of the function $\tilde{g}(a,e)$ reads as:

$$\begin{aligned} \mathcal{G}(a,e) &= \iint \tilde{g}\,\mathrm{d}a\,\mathrm{d}e \\ &= \frac{1}{r_T}\left[e\arctan\left(a(a-r_T)\tilde{g}(a,e)\right)\right. \\ &\quad \left. + \frac{a-r_T}{a}\ln\left(ae + \frac{1}{a\tilde{g}(a,e)}\right)\right] \end{aligned} \tag{50}$$

The integral in $\mathcal{I}_{a/e}$ is obtained evaluating the primitive $\mathcal{G}(a,e)$ at the two extremes of integration in semi-major, a_1 and a_2, and eccentricity, e_1 and e_2, as follows.

$$\mathcal{I}_{a/e} = \mathcal{G}(a_1,e_1) - \mathcal{G}(a_1,e_2) - \mathcal{G}(a_2,e_1) + \mathcal{G}(a_2,e_2) \tag{51}$$

Again, singular cases follow combinations of semi-major axis and eccentricity which cannot provide intersection with the target orbit. This condition verifies when either the fragments orbit perigee is larger than the target orbital radius r_T or the apogee is smaller than it. The fragments orbits leading to the singularity satisfy the following inequality:

$$e < \frac{|a - r_T|}{a} \tag{52}$$

Unfortunately, contrary to the case of inclination, the constraint of intersection in semi-major axis and eccentricity divides all the bins crossed by the function of Eq. (52) into two non-rectangular shaped volumes. As a result, the primitive $\mathcal{G}(a,e)$ cannot be found analytically. To address this problem, two alternatives were identified:

- Analytical integration in semi-major axis and eccentricity, $\mathcal{I}_{a/e}$, for the bins not crossed by the function of Eq. (52), and numerical integration through sampling otherwise.
- Analytical integration through change of variables to perigee r_p and apogee r_a radii, $\mathcal{I}_{r_p/r_a}$, over the entire domain.

Note that the integration through sampling is computationally heavy and less accurate. Therefore, since in principle the change of variable does not add complexity to the model, the first option must be chosen only if the primitive $\mathcal{G}(r_p, r_a)$ cannot be found. As demonstrated in the following, the primitive $\mathcal{G}(r_p, r_a)$ exists, even though it involves the evaluation of complex functions. This is the reason why the second option is preferred.

The change of variables $\tau(a,e)$, from semi-major axis a and eccentricity e to perigee r_p and apogee r_a radii, reads as:

$$\tau(a,e) := \begin{cases} r_p = a(1-e) \\ r_a = a(1+e) \end{cases} \tag{53}$$

To integrate in r_p and r_a, the propagated characteristics need to be interpolated in a grid defined in the new variables, to preserve the rectangular shape of the bins when crossed by the function of Eq. (52). Note that the change of variables does not modify the integrand; indeed, one should consider that the density transformation from Cartesian to Keplerian elements of Eq. (20) applies when $\boldsymbol{\alpha}$ refers to both the subset (a,e,i) and (r_p, r_a, i). This is the reason why the determinant of the Jacobian of the transformation $\tau(a,e)$ must not be added to the integration. The new integrand is simply obtained applying the change of variables of Eq. (53) to the function $\tilde{g}$, which modifies as follows.

$$\tilde{g}\left(\tau^{-1}(r_p, r_a)\right) = \frac{2}{(r_p + r_a)\sqrt{(r_p + r_a)r_T - r_p r_a - r_T^2}} \tag{54}$$

The analytical integration of Eq. (54) is not straightforward. Furthermore, the integral becomes improper when either the upper limit of r_p or the lower limit of r_a coincide with r_T, complicating even its numerical integration. Both issues can be addressed with an additional change of variables, reducing the integrand to the inverse of a hyperbolic paraboloid. Different sets of integration variables can be proposed, corresponding to different geometrical representations of the paraboloid; while some preserve the shape of the integration domain, others provide simpler expressions for the integrand. The domain-preserving case is considered first, with the change of variables:

$$\tau_X^{-1}(r_p, r_a) := \begin{cases} r_p = r_T - 2r_T X_p^2 \\ r_a = r_T + 2r_T X_a^2 \end{cases} \tag{55}$$

Each one of the new variables (X_p, X_a) depends only on one of the original variables (r_p, r_a), preserving the rectangular shape of the integration domain and the independence of the integration limits. From the physical bounds $r_p \in]0, r_T]$ and $r_a \in [r_T, \infty[$, it follows that $X_p \in [X_p(r_{p_2}), X_p(r_{p_1})] \in [0, 1/\sqrt{2}[$ and $X_a \in [X_a(r_{a_1}), X_a(r_{a_2})] \in [0, \infty[$. Introducing this change of variables and the Jacobian of the transformation into Eq. (54), integrand $\tilde{g}$ takes the form:

$$\tilde{g}\left(X_p, X_a\right) = \frac{-8}{1 + X_a^2 - X_p^2} \tag{56}$$

The integrable singularity for $r_p, r_a = r_T$ has vanished. There is still a singularity for $1 + X_a^2 - X_p^2 = 0$, but it falls out of the physical domain of the problem. After some manipulations, an analytical primitive for $\tilde{g}\left(X_p, X_a\right)$ is obtained:

$$\begin{aligned}\mathcal{G}(X_p, X_a) &= 4\left[\mathrm{Li}_2\left(X_c\right) + \mathrm{Li}_2\left(\overline{X_c}\right) - \mathrm{Li}_2\left(-X_c\right) - \mathrm{Li}_2\left(-\overline{X_c}\right)\right] \\ &= 8\Re\left[\mathrm{Li}_2\left(X_c\right) - \mathrm{Li}_2\left(-X_c\right)\right]\end{aligned} \tag{57}$$

$$X_c = -\left(X_a - \sqrt{1 + X_a^2}\right)\left(X_p + 1j\sqrt{1 - X_p^2}\right)$$

where $\overline{z}$ denotes the complex conjugate of z, $\Re[z]$ is the real part of z, and $\mathrm{Li}_2(z)$ is the dilogarithm, or Spence's function [35]:

$$\mathrm{Li}_2(z) = -\int_0^z \frac{\ln(1-u)}{u}\,\mathrm{d}u = \sum_{k=1}^{\infty}\frac{z^k}{k^2} \tag{58}$$

for complex z, where the series is convergent only for $|z| < 1$. Note that the number of dilogarithm evaluations in the last expression of Eq. (57) has been halved using the relation $\mathrm{Li}_2\left(\overline{z}\right) = \overline{\mathrm{Li}_2(z)}$. The integral $\mathcal{I}_{r_p/r_a}$ is finally obtained evaluating the primitive at the two extremes of integration in (X_p, X_a), function of the ones in (r_p, r_a):

$$\mathcal{I}_{r_p/r_a} = \mathcal{G}(X_{p_1}, X_{a_1}) - \mathcal{G}(X_{p_1}, X_{a_2}) - \mathcal{G}(X_{p_2}, X_{a_1}) + \mathcal{G}(X_{p_2}, X_{a_2}) \tag{59}$$

which involves the computation of 8 dilogarithms of complex argument.

The presence of complex arguments in Eq. (57) is related to the negative Gaussian curvature of the hyperbolic paraboloid, and cannot be avoided. However, the numerical evaluation of dilogarithms is significantly more costly for complex arguments than for real ones, so it is convenient to reduce their presence. This is achieved with a new change of variables that leverages the fact that the hyperbolic paraboloid in Eq. (56) is a rectangular one:

$$\tau_Y^{-1}(X_p, X_a) := \begin{cases} X_p = Y_y - Y_x \\ X_a = Y_y + Y_x \end{cases} \tag{60}$$

leading to a simpler integrand:

$$\tilde{g}\left(Y_x, Y_y\right) = \frac{16}{1 + 4Y_xY_y} \tag{61}$$

This change of variables introduces a functional dependency between the original variables, so the integration limits are no longer independent. The new integration domain $\mathcal{B}$ is a parallelogram, bounded by the lines for constant r_p, $Y_y^{p_{1,2}}$, and the lines for constant r_a, $Y_y^{a_{1,2}}$:

$$\begin{aligned} Y_y^{p_{1,2}} &= X_{p_{1,2}} + Y_x \\ Y_y^{a_{1,2}} &= X_{a_{1,2}} - Y_x \end{aligned} \tag{62}$$

Fig. 5 shows a schematic of the domain. While the particular values of $r_{p_{1,2}}$ and $r_{a_{1,2}}$ will change for each bin, the relative position of the lines is preserved. Moreover, $\mathcal{B}$ is always contained in the semi-infinite plane $Y_y > |Y_x|$.

Green's Theorem is used to reduce the area integral over $\mathcal{B}$ to a line integral along its boundary $\partial\mathcal{B}$:

$$\begin{aligned}\mathcal{I}_{r_p/r_a} &= \iint_{\mathcal{B}} \frac{16}{1 + 4Y_xY_y}\,\mathrm{d}Y_x\,\mathrm{d}Y_y \\ &= -4\oint_{\partial\mathcal{B}} \frac{\ln(1 + 4Y_xY_y)}{Y_x}\,\mathrm{d}Y_x\end{aligned} \tag{63}$$

The line integral has to be evaluated over the 4 boundary segments in counter-clockwise direction, substituting Y_y with the corresponding one from Eq. (62). This reduces Eq. (63) to the integral of the logarithm of a second degree polynomial of Y_x, divided by Y_x. Integration by parts allows to reduce it again to dilogarithms, involving the roots of the polynomial. For the constant r_p boundaries, the polynomial roots are complex conjugates and the primitive given as function of (X_p, X_a) is:

$$\mathcal{G}^p(X_{p_{1,2}}, X_a) = 8\Re\left[\mathrm{Li}_2\left(\left(X_{p_{1,2}} - X_a\right)\left(X_{p_{1,2}} + 1j\sqrt{1 - X_{p_{1,2}}^2}\right)\right)\right] \tag{64}$$

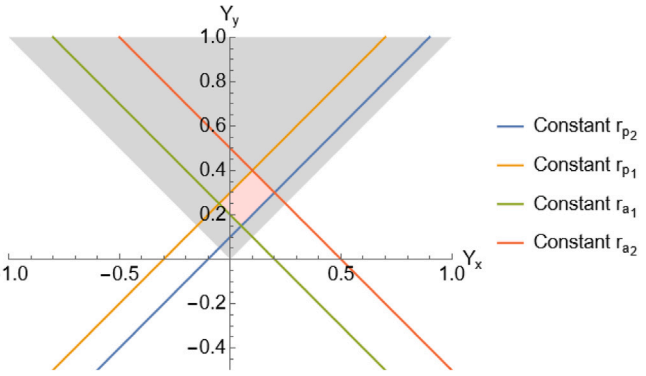

Fig. 5. Integration domain in variables (Y_x, Y_y).

Table 1
SL-16 R/B slow-varying Keplerian elements on 13th October 2010.

a [km]	e [–]	i [deg]	Ω [deg]	ω [deg]
7186	0.00090	98.31	315.59	256.72

while for the constant r_a boundaries the polynomial roots are real and the primitive is:

$$\begin{aligned}\mathcal{G}^a(X_p, X_{a_{1,2}}) = 4\Big[&\mathrm{Li}_2\left(\left(X_p - X_{a_{1,2}}\right)\left(X_{a_{1,2}} + \sqrt{1 + X_{a_{1,2}}^2}\right)\right) \\ &+ \mathrm{Li}_2\left(\left(X_p - X_{a_{1,2}}\right)\left(X_{a_{1,2}} - \sqrt{1 + X_{a_{1,2}}^2}\right)\right)\Big]\end{aligned} \tag{65}$$

Consequently, the new change of variables allows to limit the dilogarithms of complex arguments to half of the primitive evaluations. The integral $\mathcal{I}_{r_p/r_a}$ is obtained evaluating over $\partial\mathcal{B}$ in counter-clockwise direction:

$$\begin{aligned}\mathcal{I}_{r_p/r_a} = &\left[\mathcal{G}^p(X_{p_2}, X_{a_2}) - \mathcal{G}^p(X_{p_2}, X_{a_1})\right] \\ &+ \left[\mathcal{G}^a(X_{p_1}, X_{a_2}) - \mathcal{G}^a(X_{p_2}, X_{a_2})\right] \\ &+ \left[\mathcal{G}^p(X_{p_1}, X_{a_1}) - \mathcal{G}^p(X_{p_1}, X_{a_2})\right] \\ &+ \left[\mathcal{G}^a(X_{p_2}, X_{a_1}) - \mathcal{G}^a(X_{p_1}, X_{a_1})\right]\end{aligned} \tag{66}$$

involving 4 dilogarithms of complex argument and 8 of real argument, compared to the 8 dilogarithms of complex argument for Eq. (59).

4. Evaluation of the effects of occurred breakup events

This section is devoted to the application of the model presented in Section 2 and Section 3 to the evaluation of the hazard caused by two occurred fragmentation events. The first is the breakup of the US payload (P/L) NOAA-16 in Sun-Synchronous Orbit (SSO), happened at 09:50 GMT on 25$^{\text{th}}$ November 2015. The second is the fragmentation of the Russian rocket body (R/B) AMC 14 BRIZ-M on a highly elliptical orbit, which took place at 05:53 GMT on 13$^{\text{th}}$ October 2010. The effect of the fragmentation clouds is monitored in terms of impact rate and collision probability with the rocket body SL-16 in SSO, which appears in the list of 50 statistically-most-concerning derelict objects in LEO proposed by McKnight et al. [36]. For the analyses related to the first fragmentation event, the target object is assumed to follow a Keplerian motion, i.e., its orbit is considered fixed in time. Concerning the second breakup, the effect of the associated cloud of fragments on the target orbit is studied both for the cases of Keplerian or naturally evolving target orbit. The considered target slow-varying Keplerian elements are reported in Table 1. They are related to the osculating orbit of the SL-16 R/B at the epoch of the AMC 14 BRIZ-M breakup. The cross-sectional area of the target object is set to 45 m^2.

For both the fragmentation events, the density distribution at breakup epoch is firstly depicted and commented. The evolution of the

Table 2
NOAA-16 P/L Keplerian elements at fragmentation epoch.

a [km]	e [–]	i [deg]	Ω [deg]	ω [deg]	f [deg]
7226	0.00113	98.93	35.00	133.56	24.88

fragments cloud is analysed, showing the distributions at some time epochs, and the main effects of the orbital perturbations are discussed. For an easier interpretation of the dynamical evolution of the clouds, the fragments' density is depicted as function of the Keplerian elements. For the evaluation of the impact rate, the interpolation in perigee and apogee radii of the set of propagated characteristics is considered, according to the theoretical derivation presented in Section 3.2.2. The collision probability with the target object is computed under different assumptions on the cloud and target dynamics, eventually considering the complete description of the cloud in the phase space of slow-varying orbital elements and the target orbit evolution.

4.1. Effects of the NOAA-16 fragmentation in sun-synchronous orbit

This event was the second known breakup of a NOAA-series spacecraft. The payload was launched on 21st September 2000, as part of the Polar Operational Environmental Satellite series of U.S. weather satellites, and operated until 2005. The fragmentation was most likely caused by a battery explosion [37]. The spacecraft breakup generated a considerable number of fragments, 458 of which were sufficiently large to be tracked and catalogued by the Joint Space Operations Center [38]. The satellite had a mass of 1475 kg and was orbiting in a Sun-synchronous orbit. The fragmentation coordinates are reported in Table 2.

4.1.1. NOAA-16 fragments cloud evolution

The simulation here proposed considers fragments in the range 1 cm - 1 m. The number of generated fragments predicted by the NASA SBM, in case of an explosion, depends on the parameter S, as defined in [39]. Its value is set according to the expression reported in [40], where the parameter S is related to the object mass M_P as follows.

$$S = \begin{cases} k\frac{M_P\ [\text{kg}]}{10000\ [\text{kg}]} & \text{if } kM_P < 10000\ \text{kg} \\ 1 & \text{if } kM_P \geq 10000\ \text{kg} \end{cases} \tag{67}$$

with $k = 1$ for payloads and $k = 9$ for rocket bodies. Thus, for NOAA-16 P/L, the parameter S is set to 0.1475, which results in 1401 ejected fragments larger than 1 cm. Note that the simulated debris population is considerably larger than the tracked one as it also accounts for fragments with sizes that are unlikely to be observed from the ground with current technology.

Fig. 6 shows the initial density distribution in the subset of Keplerian elements (a, e, i, Ω) and area-to-mass ratio A/M. Randomisation of the cloud over argument of periapsis ω and mean anomaly M is assumed. The randomisation over ω is considered because of the small eccentricity of the parent orbit, which causes the fragments to spread almost uniformly over a range of 360 degrees in ω. On the other hand, the fast angular variable M is not accounted as interpolation variable, as the objective of this analysis is the estimation of the long-term behaviour of the debris cloud. Indeed, the difference in the fragments orbital period induces the formation of a toroid around the Earth after few orbital revolutions [31]. In Fig. 6, as well as in all the density distribution maps presented in the remainder of the paper, N represents the number of fragments in a bin with the specified coordinates.

As it can be observed, the cloud assumes the typical V-shape distribution of a LEO fragmentation in the semi-major axis-eccentricity domain. This peculiar shape is caused by the small eccentricity of the parent orbit, which bounds the fragments distribution above the curve:

$$e = \frac{|a - r_P|}{a} \tag{68}$$

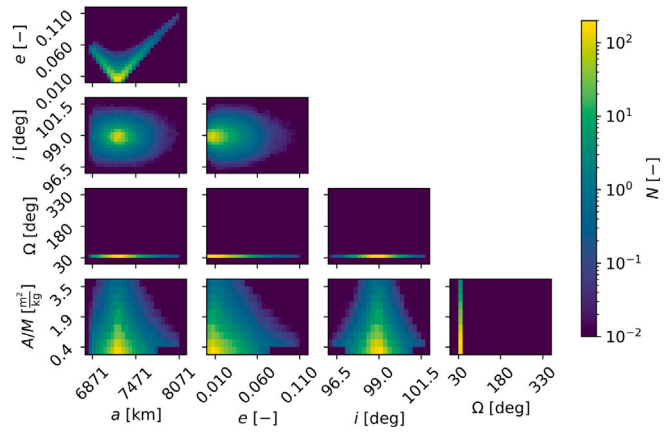

Fig. 6. NOAA-16 P/L fragmentation - Density distribution in $(a, e, i, \Omega, A/M)$ at fragmentation epoch.

with r_P orbital radius of the parent object. The curve of Eq. (68) constrains the fragments perigee and apogee to be smaller and larger than r_P, respectively. The ejected fragments distribute over a range of approximately 6 degrees in inclination and 2.5 degrees in right ascension of the ascending node. The amplitude of the cloud in i and Ω, for the case of a circular parent orbit, only depends on the latitude of the fragmentation point, with the two elements behaving in opposite ways. In particular, the closer the fragmentation occurs to the equatorial plane, the more widely the fragments spread over inclination and the narrower is the cloud domain in right ascension of the ascending node. The opposite effect results from a fragmentation near the poles. Note that in the limit cases of a fragmentation on the equatorial plane and over the poles, all the ejected fragments would share the same right ascension of the ascending node and inclination, respectively.

The debris density is propagated along 20 000 characteristics curves, whose initial conditions are uniformly extracted from the initial distribution of Fig. 6. The considered force model accounts for atmospheric drag, J_2 perturbation, solar radiation pressure and luni-solar perturbation. The 5D density distributions are retrieved according to a 1-month time discretisation, allowing to monitor both the short- and long-term dynamical behaviour of the cloud. In Fig. 7 the fragments distribution 2 months, 1 year, 5 and 15 years after fragmentation is depicted.

By looking at Fig. 7 the following considerations can be done:

- The fragments residing in the left leg of the V-shape distribution quickly re-enter the atmosphere, under the effect of a higher atmospheric density.
- As expected, the high area-to-mass ratio fragments are the most affected by atmospheric drag. As a result, the upper part of the distribution in A/M vanishes after 15 years.
- A complete randomisation over right ascension of the ascending node is not achieved even after 15 years of propagation, as some high-density regions stand out over the distribution in Ω. It is worth further noticing that after 1 year the fragments with the highest rate of change in Ω have not yet reached the slowest ones. This proves the need of characterising the fragments density in right ascension of the ascending node.
- The inclination of the fragments is barely affected by solar radiation pressure and luni-solar perturbation, because of the limited force exerted by the two disturbances below 1000 km altitude, where most of the fragments are found.

4.1.2. Collision risk from a 1D fragments cloud in orbital radius

The impact rate is computed averaging the fragments flux against the target cross-sectional area, over the target mean anomaly, according

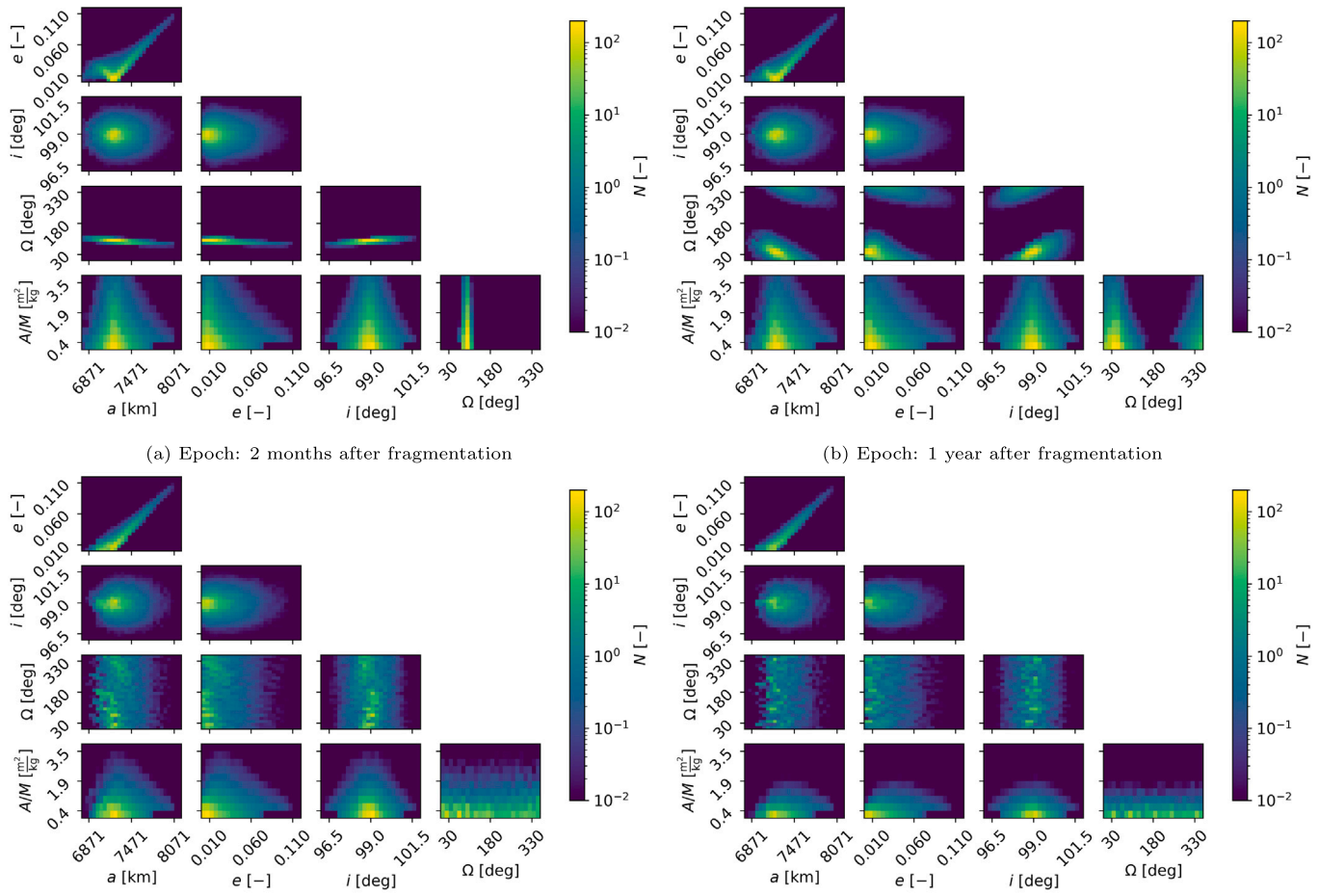

(a) Epoch: 2 months after fragmentation

(b) Epoch: 1 year after fragmentation

(c) Epoch: 5 years after fragmentation

(d) Epoch: 15 years after fragmentation

Fig. 7. NOAA-16 P/L fragmentation - Density distribution in $(a, e, i, \Omega, A/M)$ over time.

to Eq. (17). The 1D spatial density function n_r is retrieved from the 4D distribution in Keplerian elements through the Keplerian to Cartesian coordinates transformation, and it varies discretely with orbital radius r, as a result of a 1D interpolation through binning with step-size $\delta r = 50$ km. Following the approach proposed in [20], to compute the average impact velocity of Eq. (8), the fragments orbits are assumed to have the same inclination as the parent one. As a result, the average impact velocity v_{rel}, as well as its product with the latitude-dependent function β, remain constant over time, as they do not depend on the evolution of the fragments distribution. Therefore, the average impact velocity is only responsible for the impact rate magnitude, while its trend over time t is only dependent on the evolution of the spatial density function, evaluated at the target orbital radius r_T, $n_r(t, r_T)$. Fig. 8(a) shows the impact velocity as function of the target argument of latitude u_T. Figs. 8(b) and 8(c) depict the associated values of difference in right ascension of the ascending node $\Delta\Omega$ and angle between fragments and target velocity vectors δ, computed through Eq. (5) and (7), respectively. The subscripts $(\cdot)_1$ and $(\cdot)_2$ identify the two possible solutions of intersection. Note that the incorrect solutions, which result from considering $\Delta\Omega$ and M_T as linearly related [20], corresponding to Eq. (6), are also displayed with the red dashed line.

As it can be inferred, the different approach between the model in [20] and the newly proposed method dramatically changes the resulting profile of the impact velocity. It is worth noticing that, for a narrow range of values of the target argument of latitude u_T, no solution is found. Indeed, since the target covers a wider range in latitude, because of its lower inclination with respect to the parent orbit, there exist values of u_T for which the target latitude is greater than the fragments one, for any value of the fragments argument of latitude u. As a result, no intersection is geometrically possible. Fig. 9 depicts the evolution of the spatial density function over time, as function of altitude h and latitude ϕ.

Combining the results of Figs. 9 and 8(a), the profile of the impact rate can be obtained and, as a consequence, the estimated collision probability, according to the Poisson distribution of Eq. (2). The two profiles as function of time are shown in Fig. 10.

As it can be noted, the decrease of the impact rate over time comes as a consequence of the lowering of the spatial density function at $r = r_T$, caused by the effect of atmospheric drag.

4.1.3. Collision risk from a 3D fragments cloud in r_p, r_a, i

The propagated characteristics are here interpolated in the 3D phase space (r_p, r_a, i), according to the following step-sizes: $\delta r_p = \delta r_a = 50$ km, $\delta i = 0.25$ deg. Hence, the density distribution is randomised over right ascension of the ascending node. As a result, the associated spatial density function is constant over longitude λ. Nevertheless, two main improvements are added with respect to the solution proposed in Section 4.1.2, namely:

- The characterisation of the fragments in inclination allows the accurate estimation of the spatial distribution over latitude ϕ.
- From the distribution of the fragments in the independent orbital elements (r_p, r_a, i), the impact velocity can be computed as a discrete function of both phase space and time. As demonstrated in Section 3.2.1, if the grid is fine enough, the accuracy of the model is guaranteed.

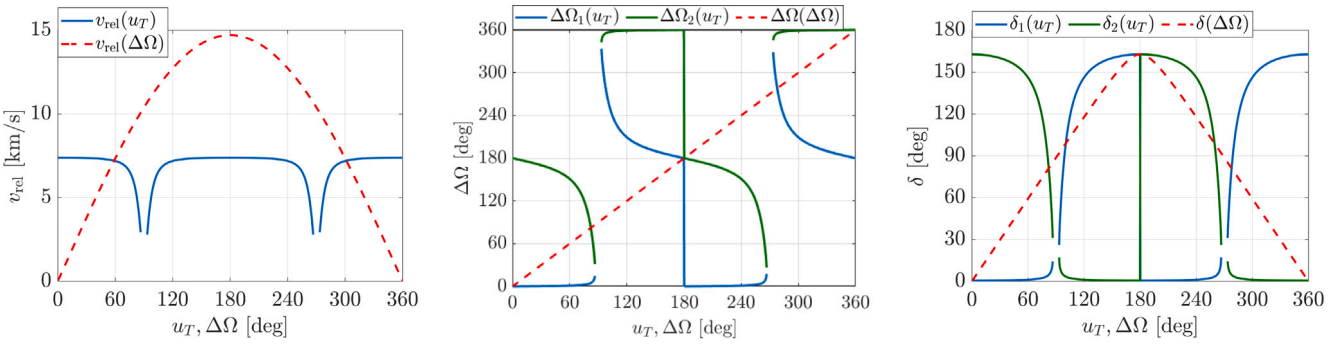

(a) Impact velocity v_{rel} (b) Difference in right ascension of the ascending node $\Delta\Omega$ (c) Angle between the velocity vectors δ

Fig. 8. NOAA-16 P/L fragmentation - Impact velocity v_{rel}, difference in right ascension of the ascending node $\Delta\Omega$, and angle between fragments and target velocity vectors δ as function of the target argument of latitude.

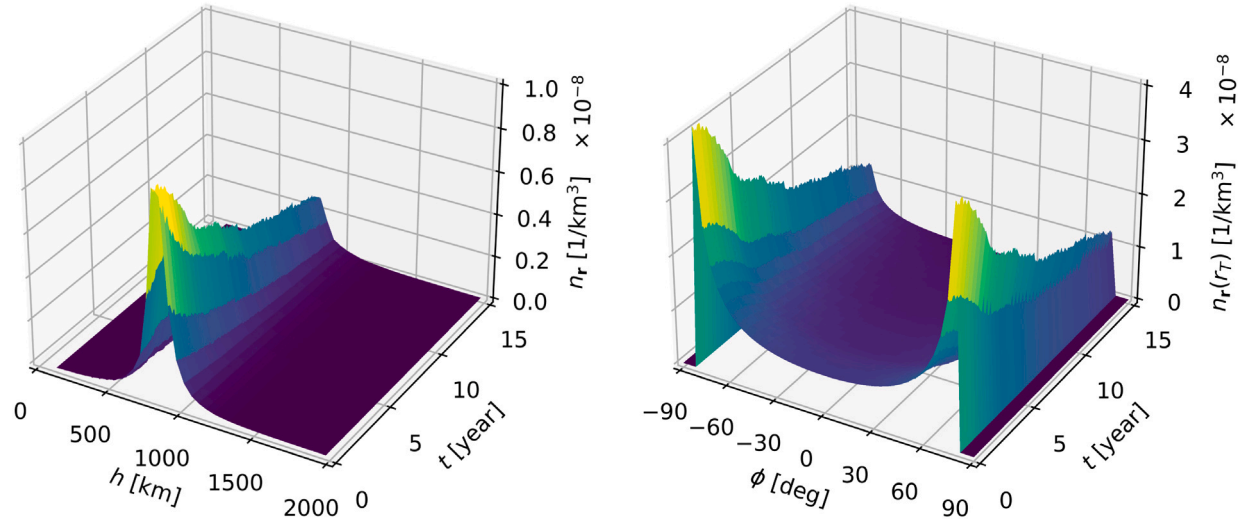

(a) Dependency on altitude (b) Dependency on latitude

Fig. 9. NOAA-16 P/L fragmentation - Spatial density as function of altitude, latitude, and time.

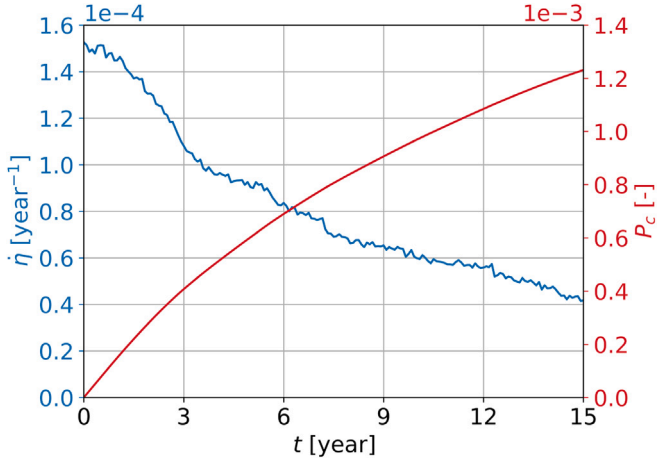

Fig. 10. NOAA-16 P/L fragmentation - Impact rate and collision probability with SL-16 R/B over time from the 1D spatial density function.

The validity of this second point for the considered discretisation is here verified. As derived in Section 3.2.1, the accuracy degradation introduced by the assumption of bin-wise constant impact velocity is proportional to the ratio $\xi = \Delta v / v_{rel}$, with Δv velocity difference between the bin centre and a generic point in the bin, and v_{rel} relative velocity with the target object measured at the bin centre. Fig. 11 shows the maximum percentage value of ξ, $\xi_{\%}^{max}$, within rectangular-shaped volumes with dimensions equal to the step-sizes δr_p, δr_a and δi, as function of their location in the (r_p, r_a) domain occupied by the evolving fragments cloud that guarantees intersection with the target object. The inclination is set equal to the one of the parent orbit, i_P, as its value has minimal effect on the results. Note that, for every point, only the three independent orbital elements $\boldsymbol{\alpha} := (r_p, r_a, i)$ are specified, while the remaining three elements $\boldsymbol{\beta} := (\Omega, \omega, f)$ are retrieved by imposing intersection with the target object. This procedure is possible if a fixed target object position, $\boldsymbol{r}_T$, is considered. For the results of Fig. 11, the target object is assumed to be located at the ascending node. As it can be inferred, the error introduced by the considered assumption is negligible.

Fig. 12 shows the effect of the improvements with respect to the 1D formulation. In particular, Fig. 12(a) displays the normalised cumulative distribution of fragments at fragmentation epoch as function of the latitude ϕ, CDF_ϕ, resulting from the different modelling of the debris cloud. It is computed as follows.

$$\mathrm{CDF}_\phi = \frac{1}{N} \int_{-\pi/2}^{\phi} \int_{0}^{2\pi} \int_{R_E}^{\infty} n_{\boldsymbol{r}} \, \mathrm{d}r \, \mathrm{d}\lambda \, \mathrm{d}\phi \tag{69}$$

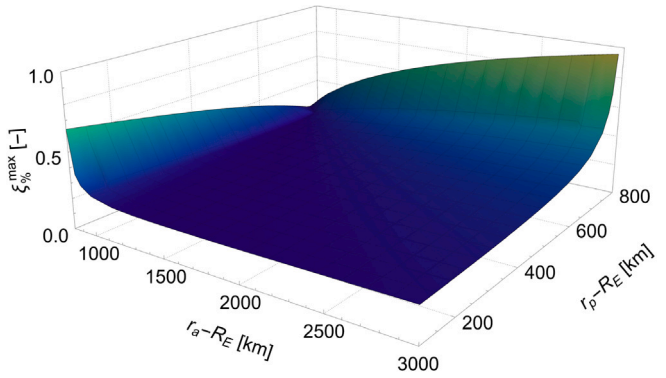

Fig. 11. NOAA-16 P/L fragmentation - Maximum percentage ratio ξ as function of the bin coordinates in the perigee radius-apogee radius domain. In the figure, R_E is the Earth mean radius.

with N total number of fragments and R_E Earth mean radius. Note that the dashed red line is the percentage error of the 1D formulation with respect to the 3D model, computed according to the following relation:

$$\mathrm{Err}^{\mathrm{CDF}_\phi}_{\%} = 100 \cdot (\mathrm{CDF}^{\mathrm{3D}}_\phi - \mathrm{CDF}^{\mathrm{1D}}_\phi) \tag{70}$$

As it can be observed, the 1D formulation underestimates the number of fragments at high latitudes; this result is expected, as all the fragments are assumed to share the same inclination as the parent one, which constrains them to distribute over the following range in latitude:

$$\begin{cases} \Delta\phi = [-i, i] & \text{if } i \leq \frac{\pi}{2} \\ \Delta\phi = [i - \pi, \pi - i] & \text{if } i > \frac{\pi}{2} \end{cases} \tag{71}$$

On the contrary, as part of the fragments are actually injected on orbits with lower inclination with respect to the parent one (Fig. 6), the 3D distribution covers a wider range in latitude. As a result, since the total integral of the density is preserved between the two formulations, the 1D model overestimates the number of fragments at low latitudes.

Instead, Fig. 12(b) shows a comparison in terms of estimated average impact velocity as function of the target argument of latitude u_T. As it can be noted, the characterisation of the fragments over inclination allows the debris cloud to potentially impact the target, for any value of u_T. It is also worth observing that the 3D model estimates an average impact velocity higher than the 1D model, for any target position along its orbit. The error on the relative velocity, represented by the red dashed line on the plot, is monitored through the following relation:

$$\mathrm{Err}^{v_{\mathrm{rel}}}_{\%} = 100 \cdot \frac{v^{\mathrm{3D}}_{\mathrm{rel}} - v^{\mathrm{1D}}_{\mathrm{rel}}}{\max_{u_T}\left(v^{\mathrm{3D}}_{\mathrm{rel}}\right)} \tag{72}$$

The impact rate is here computed directly from the density in orbital elements, according to Eq. (29). Note that, as the distribution is randomised over the angles (Ω, ω, M), the density value is dependent on the subset of orbital elements $\boldsymbol{\alpha}$ only; hence, the phase space density $n_{\alpha,\beta}$ can be taken outside of the inner summation. Fig. 13 shows the impact rate and the probability of collision as function of time.

As it can be observed, the cumulative collision probability after 15 years is lower than the one predicted by the 1D model reported in Fig. 10. Again, the result was expected; indeed, the 3D formulation estimates a higher number of fragments at high latitudes, where the average impact velocity is low (the minima of the impact velocity v_{rel} are monitored at u_T equal to either 90 deg or 270 deg). On the contrary, the high impact velocity region is occupied by a lower concentration of fragments with respect to the 1D model. As the impact rate comes as a combined effect of impact velocity and debris density, an overall lower probability of collision is estimated.

To further validate the model, the impact rate and collision probability profiles of Fig. 13 are computed through the well-known impact estimation method proposed by Kessler [10]. According to this theory, the impact rate $\dot{\eta}_j$ between a spacecraft with orbital radius r_T, longitude λ_T, and latitude ϕ_T at a given time t and an orbiting object with fixed semi-major axis a, eccentricity e and inclination i, and equally probable longitude of the node and argument of periapsis, is found as [10]:

$$\begin{aligned} \dot{\eta}_j &= v_{\mathrm{rel}} \sigma \, n_{\boldsymbol{r}}(r_T, \lambda_T, \phi_T) \\ &= \frac{v_{\mathrm{rel}} \sigma}{4\pi^3 r_T a^2 \sqrt{e^2 - \left(\frac{r_T}{a} - 1\right)^2} \sqrt{\sin^2 i - \sin^2 \phi_T}} \end{aligned} \tag{73}$$

where v_{rel} is the average velocity of the four solutions of intersection of Eq. (25), and σ is the collision cross-sectional area, which is here assumed to coincide with the target object one, A_c. To estimate the collision risk posed by the debris cloud, the 3D fragments distribution is sampled and the overall impact rate is computed by summing up the contribution of each fragment according to Eq. (73), i.e.:

$$\dot{\eta} = \sum_j \dot{\eta}_j \tag{74}$$

Finally note that Eq. (73) provides an estimate of the impact rate for a fixed position of the target object. Therefore, the average impact rate with the object over a complete revolution around the Earth is computed through Eq. (18). Fig. 14 shows a comparison of both impact rate and collision probability profiles obtained from the 1D distribution in orbital radius r, 3D distribution in (r_p, r_a, i) and samples-based Kessler formulation. For this latter case, a population of 100000 samples is extracted from the 3D distribution. It can be inferred how the results obtained with the Kessler formulation show a similar trend to the 3D density-based model.

4.1.4. Collision risk from a 4D fragments cloud in orbital elements r_p, r_a, i, Ω

The collision probability is finally computed accounting for the debris distribution over right ascension of the ascending node Ω, further discretising the fragments density of Section 4.1.3 in Ω according to a step-size $\delta\Omega = 15$ deg. This means that, for a given subset of orbital elements $\boldsymbol{\alpha}$ and fixed target position $\boldsymbol{r}_T$, there exist two possible density values $n_{\boldsymbol{\alpha},\beta}$ associated to the orbits with right ascension Ω_1, Ω_2 of Eq. (25), guaranteeing intersection. As a result, the cloud evolution in Ω is expected to massively impact on the profile of the impact rate. Note that the characterisation of the debris cloud over right ascension of the ascending node implies that the fragments are no longer uniformly spread in longitude λ. Fig. 15 depicts the impact rate and the probability of collision with rocket body SL-16 as function of time.

As it can be observed, the profile of the impact rate has dramatically changed. It is now characterised by an oscillatory behaviour over time with a characteristic period of roughly 1 year, whose amplitude decreases over time. The reason for these oscillations can be understood by looking at the evolution of the spatial density as function of longitude λ and latitude ϕ over time, relative to the fixed target orbit, reported in Fig. 16. Note that the distributions refer to the epochs $t_0, \ldots, t_5$ highlighted in Fig. 15.

The randomisation process over right ascension of the ascending node is clearly observable. Note that at epoch t_2 a unique high-density region still stands out from the fragments distribution. After the 15 years propagation, even though the distribution is more uniform over longitude, some high-density orbits can be still distinguished. The maxima in the impact rate profile (epochs t_2 and t_3) verify when the most crowded orbits have a shift of 180 deg in right ascension of the ascending node Ω with respect to the target. Instead, when they share the same Ω as the target (epochs t_1 and t_4) a minimum is found in the impact rate evolution. Note that the maxima (and minima) occur every 1 year because, since the fragments move on a quasi-SSO orbit,

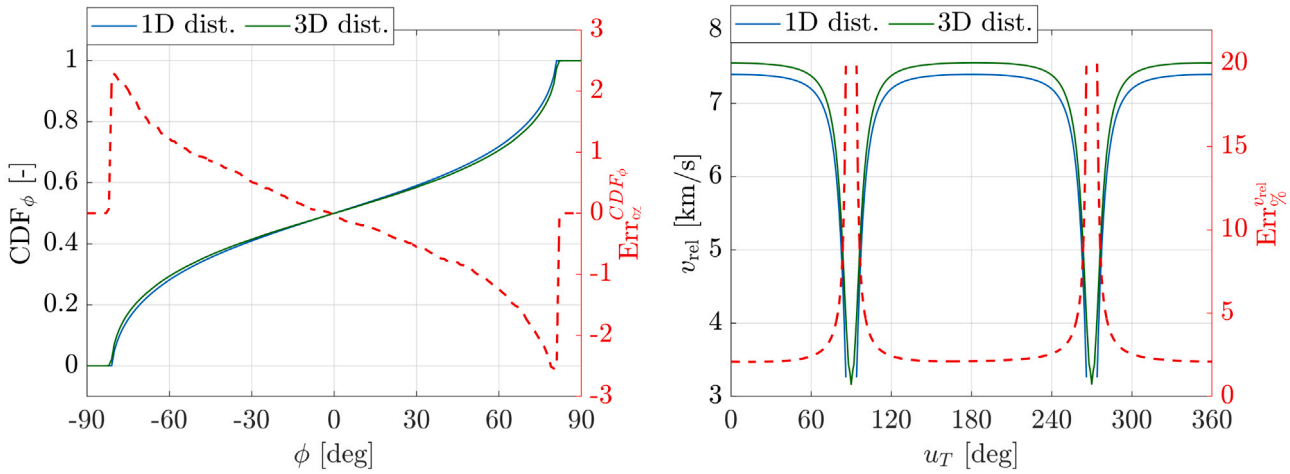

(a) Normalised cumulative number of fragments as function of latitude

(b) Impact velocity as function of target argument of latitude

Fig. 12. NOAA-16 P/L fragmentation - Comparison between 1D and 3D formulations.

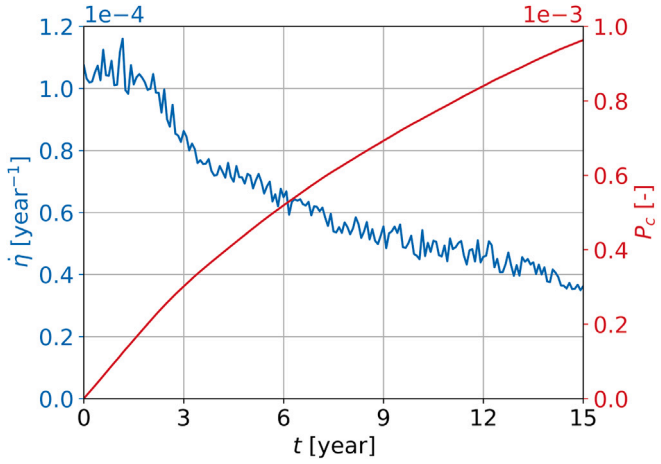

Fig. 13. NOAA-16 P/L fragmentation - Impact rate and collision probability with SL-16 R/B over time from the 3D phase space density function.

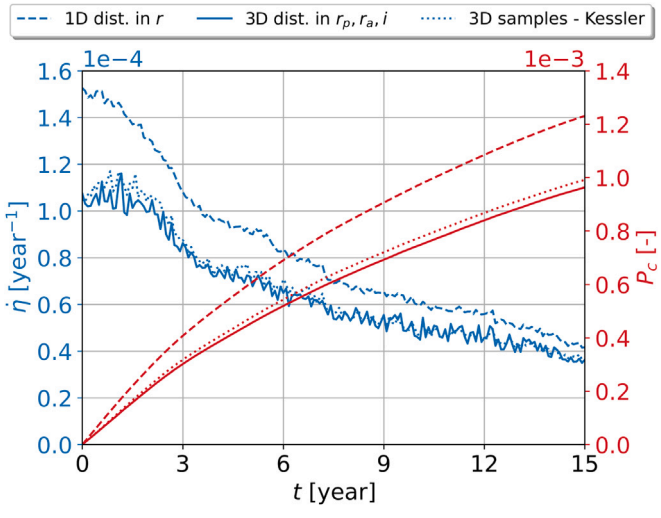

Fig. 14. NOAA-16 P/L fragmentation - Impact rate and collision probability with SL-16 R/B over time from the 1D spatial density function, 3D phase space density function and samples-based Kessler formulation.

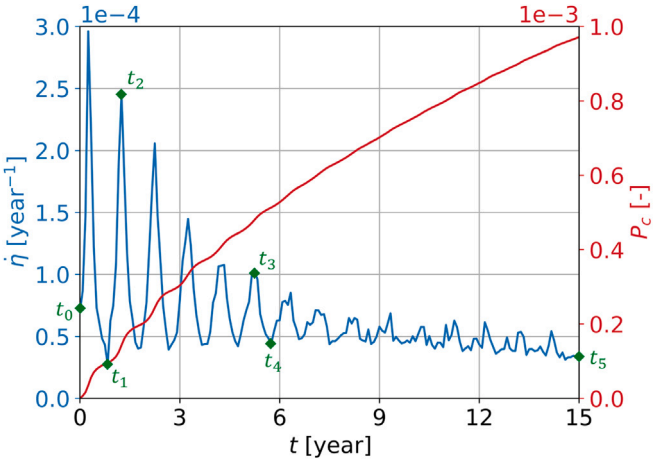

Fig. 15. NOAA-16 P/L fragmentation - Impact rate and collision probability with SL-16 R/B over time from the 4D phase space density function.

Table 3
AMC 14 BRIZ-M R/B Keplerian elements at fragmentation epoch.

a [km]	e [–]	i [deg]	Ω [deg]	ω [deg]	f [deg]
19981	0.64859	48.94	195.24	287.15	31.97

the rate of change $\dot{\Omega}$ is roughly 360 deg/year. The decrease in the amplitude of oscillation is a consequence of the randomisation over right ascension of the ascending node, which causes the target to move over an increasingly evenly distributed debris cloud in longitude.

4.2. Effects of the AMC 14 BRIZ-m fragmentation in highly elliptical orbit

The fragmentation event occurred 31 months after launch, when the rocket body was orbiting on a highly elliptical orbit [38]. The cause was identified in a malfunction of the propulsion system. The Space Surveillance Network (SSN) catalogued 116 large fragments, even though they were supposed to be many more [38]. Indeed, the parent orbit perigee was located in the southern hemisphere, out of the SSN coverage, which made the tracking of the ejected fragments difficult. The Keplerian elements of the rocket body at fragmentation epoch are reported in Table 3. The object had a mass of 2510 kg [38].

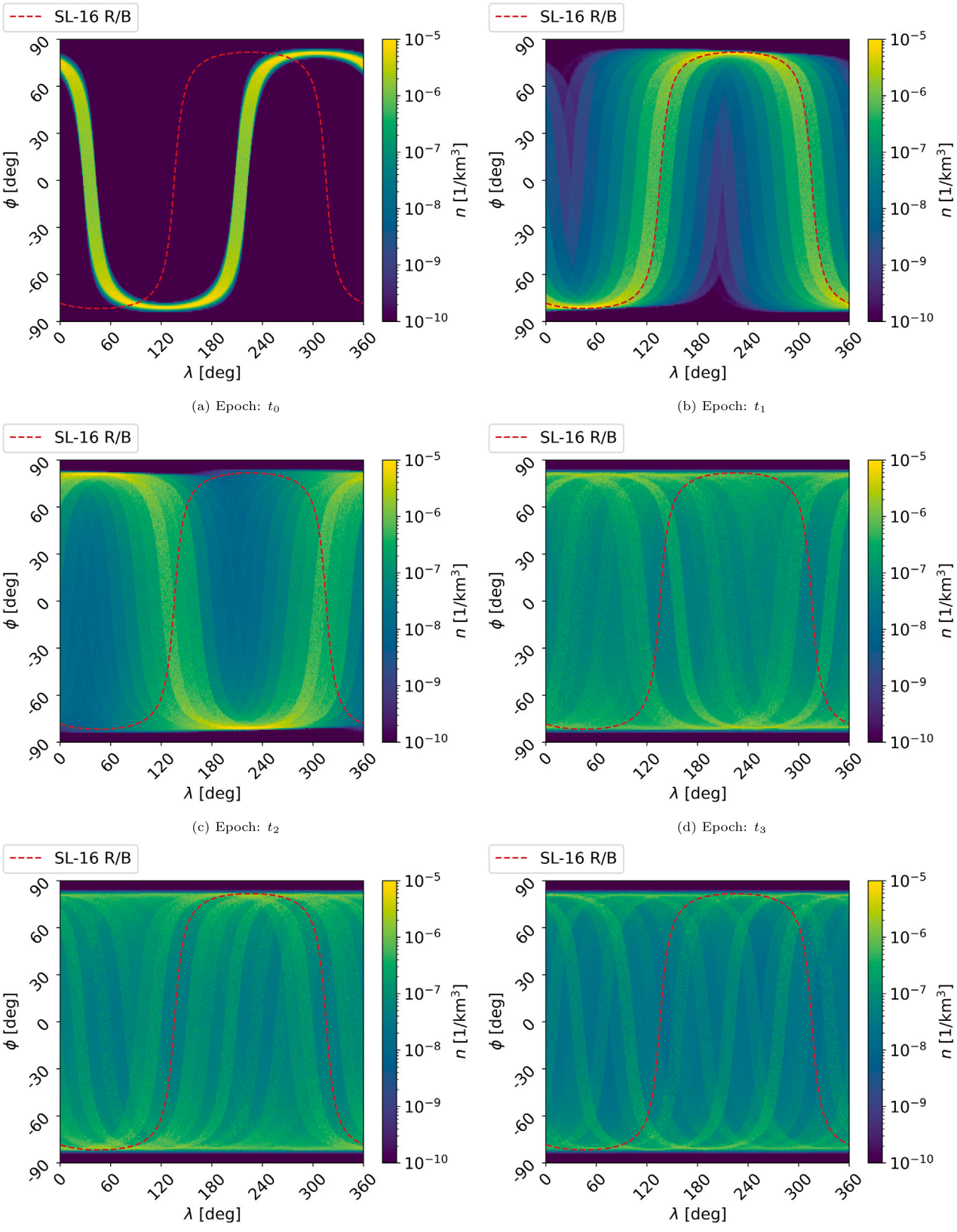

(a) Epoch: t_0

(b) Epoch: t_1

(c) Epoch: t_2

(d) Epoch: t_3

(e) Epoch: t_4

(f) Epoch: t_5

Fig. 16. NOAA-16 P/L fragmentation - Spatial density as function of longitude λ and latitude ϕ over time.

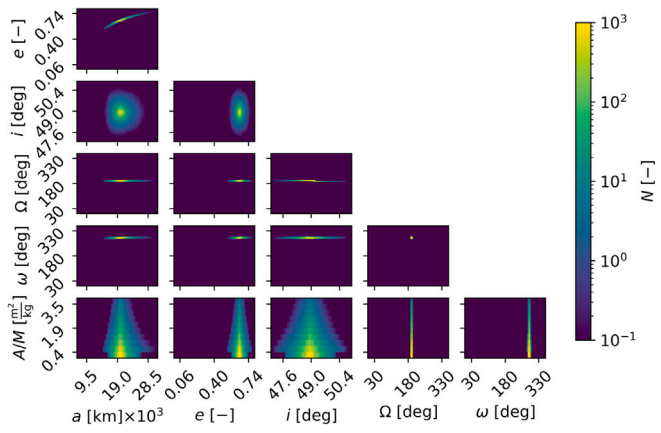

Fig. 17. AMC 14 BRIZ-M R/B fragmentation - Density distribution in $(a, e, i, \Omega, \omega, A/M)$ at fragmentation epoch.

4.2.1. AMC 14 BRIZ-M fragments cloud evolution

As for the previous fragmentation scenario, fragments in the range 1 cm - 1 m are considered. According to the object mass and type, the explosion results in 9503 ejected fragments [39]. Fig. 17 shows the initial density distribution in the phase space of slow-varying Keplerian elements $(a, e, i, \Omega, \omega)$ and area-to-mass ratio A/M. As always, the debris cloud is assumed to be randomised over mean anomaly.

As it can be observed, the cloud covers a much wider range in semi-major axis and eccentricity; indeed, the higher is the parent specific orbital energy, the easier it is to modify the orbit shape. Instead, the fragments occupy a tiny domain over both right ascension of the ascending node and argument of periapsis. Fig. 18 depicts the fragments distribution 2 months, 1 year, 5 and 15 years after fragmentation, resulting from the propagation of the debris density along 20 000 characteristic lines. The same force model as in Section 4.1.1 is considered.

It is worth underlining the following differences with respect to the fragmentation scenario described in Section 4.1:

- The debris cloud is far from being randomised over right ascension of the ascending node Ω and argument of periapsis ω, even after 15 years of propagation. On the contrary, in the (Ω, ω) phase space, the fragments distribute over a diagonal line, which gets thicker and thicker as time passes. As demonstrated in [24], the angular coefficient of this line-like distribution can be approximated as the ratio between the long-term rate of change $\dot{\Omega}$ and $\dot{\omega}$, caused by the J_2 perturbation.
- Third-body perturbation and solar radiation pressure notably affect the cloud evolution in eccentricity and inclination.
- Despite the low-altitude of the parent orbit perigee, only a small fraction of the debris cloud is considerably affected by atmospheric drag. As a result, only the fragments with the highest area-to-mass ratio re-enter the atmosphere over the 15 years propagation time.

4.2.2. Collision risk from a 5D fragments cloud in orbital elements r_p, r_a, i, Ω, ω

The collision probability is here computed considering the debris distribution over the slow-varying orbital elements $(r_p, r_a, i, \Omega, \omega)$, discretised according to the following step-sizes: $\delta r_p = 50$ km, $\delta r_a = 500$ km, $\delta i = 0.25$ deg, $\delta\Omega = \delta\omega = 5$ deg. As a result, the summation of Eq. (29) is carried out over the four possible intersecting orbits, according to the two values of right ascension of the ascending node Ω_1 and Ω_2, and to the four values of argument of periapsis $\omega_1, \dots, \omega_4$. Following the same approach of Section 4.1.3, the validity of the assumption of bin-wise constant impact velocity is verified also in this second analysis.

Fig. 19 depicts the behaviour of the maximum percentage value of the ratio ξ, $\xi_{\%}^{\max}$, as function of perigee and apogee radii, over the domain occupied by the fragmentation cloud generated from the explosion of AMC 14 BRIZ-M R/B and providing intersection with the target object. As it can be observed, despite a slightly higher inaccuracy, confined in two narrow areas, due to the coarser discretisation in apogee radius r_a, δr_a, the validity of the considered approximation is confirmed.

The profiles of the impact rate and collision probability over time are reported in Fig. 20. Again, for a better comprehension of the results, the spatial density function at the epochs highlighted in Fig. 20 is also shown in Fig. 21.

As it can be noticed, the impact rate, after a narrow peak within the first year of cloud evolution, is almost null for a period of approximately 4 years. Indeed, note that the fragments inclination guarantees a considerably smaller coverage over latitude compared to the case of NOAA-16 P/L breakup. Thus, the intersection with the target is possible for a limited range of longitude values $\lambda \in \mathcal{D}_\lambda$. In addition, the fragments move on highly eccentric orbits and the cloud is randomised neither in longitude of the nodes nor in argument of periapsis, which means that only a small part of the distribution is in the altitude range covered by the target. In order for the fragments to possibly impact the target, the following condition must verify:

$$\exists \lambda \in \mathcal{D}_\lambda \; : \; n_{\mathbf{r}}(r_T, \lambda) \neq 0 \tag{75}$$

At time t_2, the debris cloud is at the target altitude for $\lambda \in [30, 110]$ deg. However, for such values of longitude, the target latitude is outside the range covered by the cloud. As a result, no intersection is geometrically possible. In other words, the zero-impact rate period of Fig. 20 coincides with the time needed for the main bulk of fragments to reacquire an orbital plane and orientation capable of providing intersection with the target orbit. Note that, as time passes, even though the high-density orbits can be still distinguished in the spatial distribution over altitude h and longitude λ, the cloud covers a wider and wider range of longitude values, at the target altitude, eventually spreading over the entire domain of 360 deg. When this condition verifies, a non-null impact rate is always obtained. Note that, because of the very slow randomisation process, if the propagation time were increased, the profile of the impact rate would be characterised by notable oscillations, which would be attenuated in a much longer period of time compared to the case of Fig. 15.

4.2.3. Collision risk with a naturally evolving target

As a last analysis, the natural evolution of the target orbit is also taken into account in the assessment of the collision risk with the debris cloud. Note that this additional feature is of crucial importance; indeed, one should consider that the objects causing the highest hazard for the proliferation of space debris are uncontrolled derelicts as rocket bodies or mission related objects [36], which naturally evolve under the effect of orbital perturbations.

The Keplerian elements of the target object SL-16 R/B are propagated under the same dynamical model adopted for the debris cloud. The average impact rates and collision probabilities, computed every 1 month, are evaluated considering the target Keplerian elements propagated at the same time epoch. Fig. 22 shows the resulting profiles of impact rate and collision probability with SL-16 R/B.

Even though the profile of the impact rate is now the result of the relative evolution of debris cloud and target orbit, it can be immediately inferred that the precession of the target orbit node is driving the profile; indeed, the peaks in the impact rate are found with an approximately 6-months repetition, which coincides with half revolution of the node for a Sun-synchronous orbit. Note that the profile is characterised by several zero-impact rate periods, which are found until the cloud covers the 360 deg range in longitude, at the target altitude, as explained in Section 4.2.2. As the fragments get more spread over right ascension of the ascending node and argument of periapsis, the oscillations reduce in amplitude.

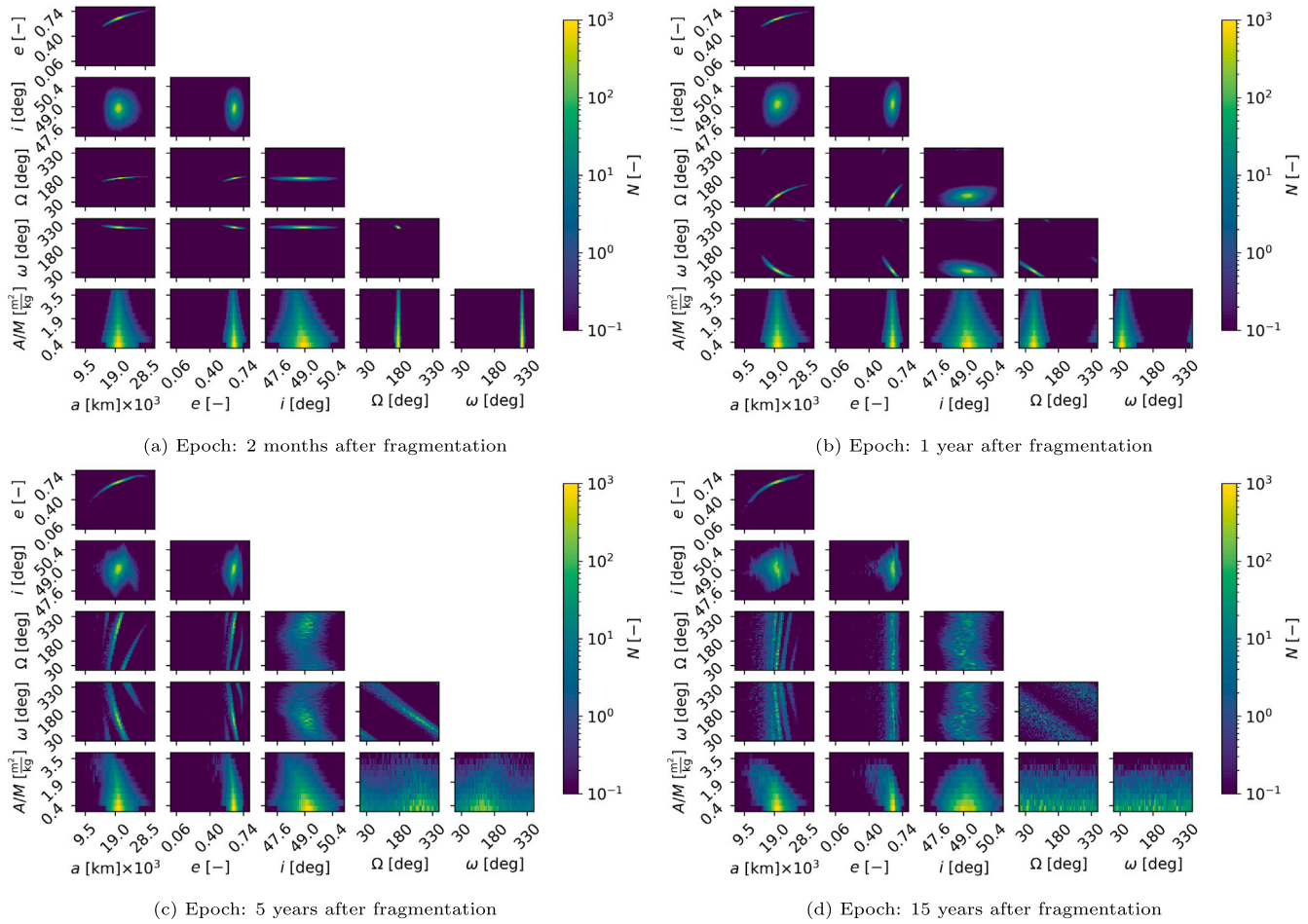

(a) Epoch: 2 months after fragmentation

(b) Epoch: 1 year after fragmentation

(c) Epoch: 5 years after fragmentation

(d) Epoch: 15 years after fragmentation

Fig. 18. AMC 14 BRIZ-M R/B fragmentation - Density distribution in $(a, e, i, \Omega, \omega, A/M)$ over time.

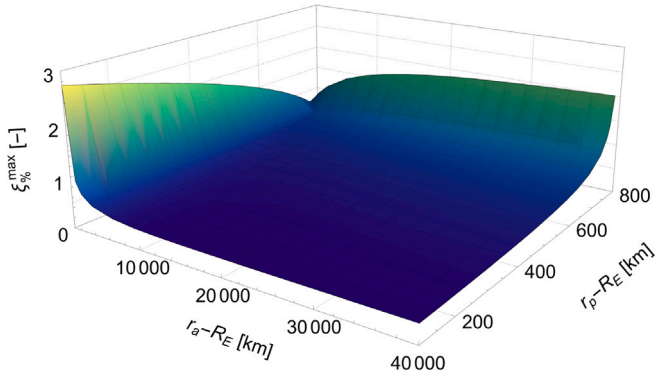

Fig. 19. AMC 14 BRIZ-M R/B fragmentation - Maximum percentage ratio ξ as function of the bin coordinates in the perigee radius-apogee radius domain.

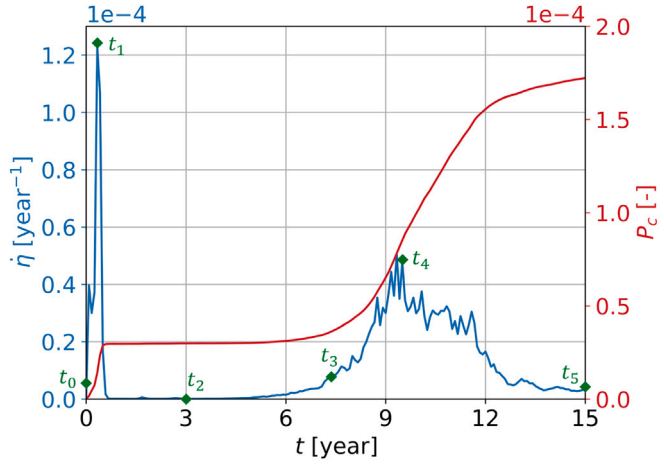

Fig. 20. AMC 14 BRIZ-M R/B fragmentation - Impact rate and collision probability with SL-16 R/B over time from the 5D phase space density function.

5. Conclusions

The evaluation of the collision risk posed by fragmentation clouds, evolving under any complex dynamics, is a delicate task. Historically, this objective was achieved via semi-deterministic approaches, which suffer of a high computational cost when centimetre- or millimetre-sized particles are modelled. On the other hand, the more efficient probabilistic methods demanded the introduction of simplifying assumptions on the orbital dynamics and impact geometry between fragments and target satellite. This paper proposed a new density-based formulation for an efficient and accurate estimation of the collision hazard caused by a debris cloud, described through a multi-dimensional phase space density function in orbital elements. The probabilistic debris cloud propagation model, derived in a previous work by the authors, was adopted to compute the evolution of the fragments density over time. The resulting phase space density function, which discretely varies over both space and time, was provided as input to the collision

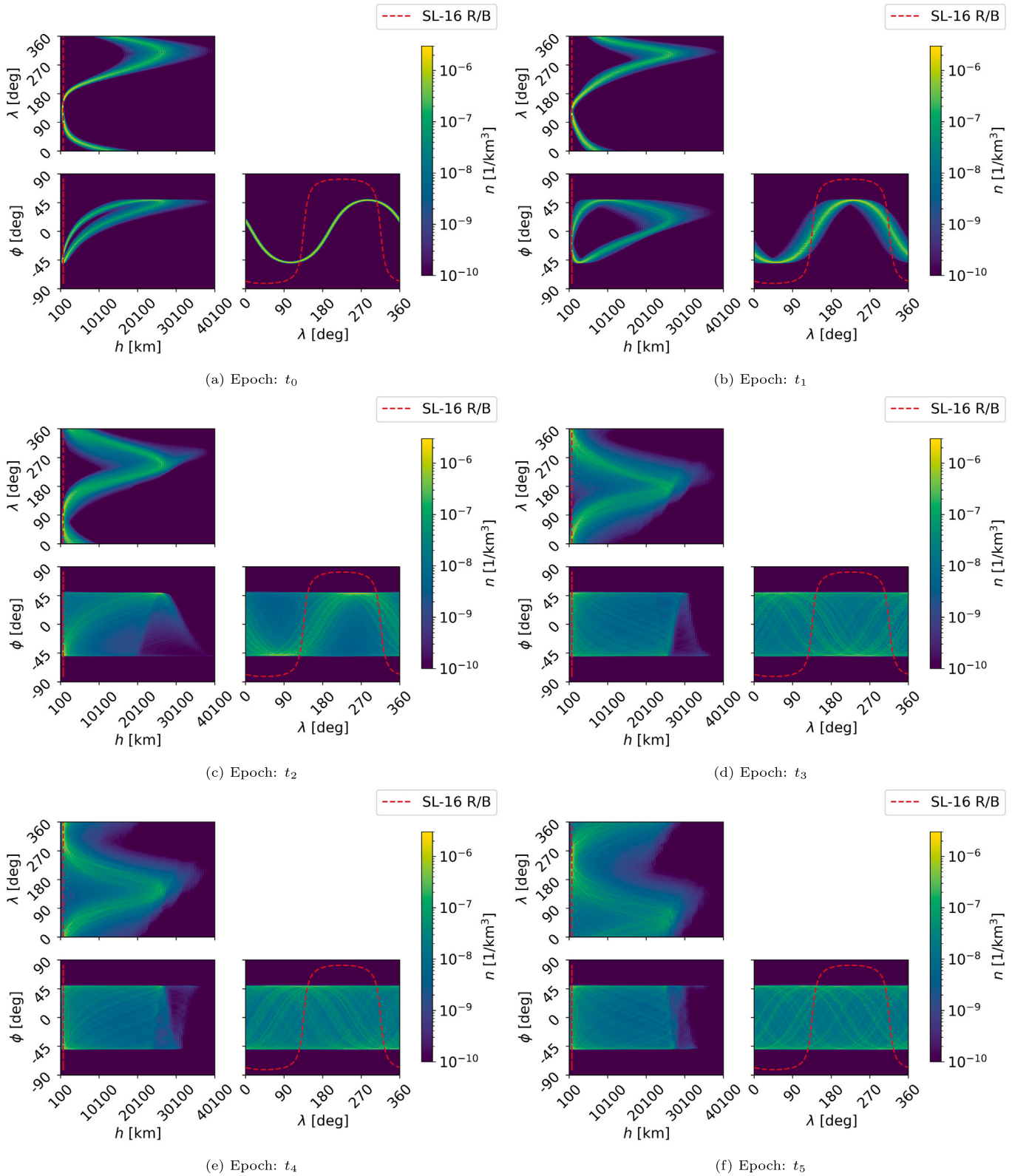

(a) Epoch: t_0

(b) Epoch: t_1

(c) Epoch: t_2

(d) Epoch: t_3

(e) Epoch: t_4

(f) Epoch: t_5

Fig. 21. AMC 14 BRIZ-M R/B fragmentation - Spatial density as function of altitude h, longitude λ and latitude ϕ over time.

risk model. This part was the core of the paper. A novel approach for the estimation of the impact rate with a target satellite was presented here. It analytically transforms the six-dimensional phase space density function into the three-dimensional spatial density function, needed for the evaluation of the flux of fragments over the target area. The impact velocity was approximated as bin-wise constant, as it was mathematically demonstrated to only slightly affect the accuracy of the method. The resulting analytical formulation guarantees flexibility to the modelling of any impact geometry in any arbitrarily complex orbital regime, as well as greater efficiency with respect to semi-deterministic approaches. The model was applied to the evaluation of the collision risk posed by occurred fragmentation events on an uncontrolled rocket

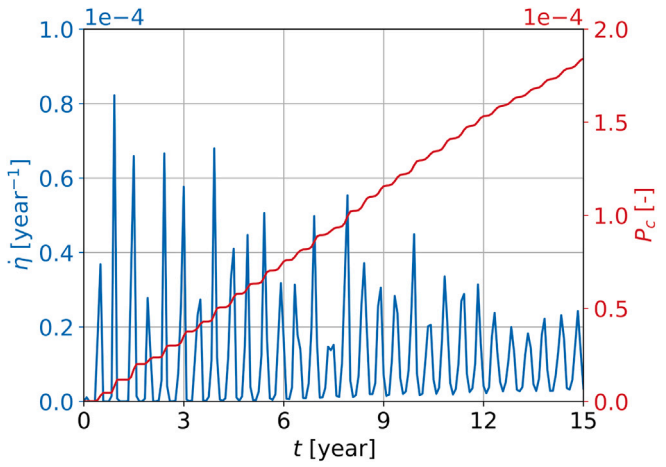

Fig. 22. AMC 14 BRIZ-M R/B fragmentation - Impact rate and collision probability with SL-16 R/B over time from the 5D phase space density function. Target orbit evolution included.

body. The additional dynamical features, which the model is able to characterise with respect to previous probabilistic formulations, were consecutively included and discussed.

Declaration of competing interest

The authors declare that they have no known competing financial interests or personal relationships that could have appeared to influence the work reported in this paper.

Acknowledgements

This project has received funding from the European Research Council (ERC) under the European Union's Horizon 2020 research and innovation programme (grant agreement No 101089265 - GREENSPECIES) and from the European Space Agency, France contract 4000133981/21/D/KS.

References

[1] ESA Space Debris Office, ESA's Annual Space Environment Report, Tech. rep., 2023.
[2] H. Klinkrad, Space Debris: Models and Risk Analysis, Springer Science & Business Media, 2006.
[3] A.E. White, H.G. Lewis, The many futures of active debris removal, Acta Astronaut. 95 (2014) 189–197, http://dx.doi.org/10.1016/j.actaastro.2013.11.009, URL https://www.sciencedirect.com/science/article/pii/S0094576513004013.
[4] G. Drolshagen, Impact effects from small size meteoroids and space debris, Adv. Space Res. 41 (2008) 1123–1131, http://dx.doi.org/10.1016/j.asr.2007.09.007.
[5] H. Krag, M. Serrano, V. Braun, P. Kuchynka, M. Catania, J. Siminski, M. Schimmerohn, X. Marc, D. Kuijper, I. Shurmer, A. O'Connell, M. Otten, I. Muñoz, J. Morales, M. Wermuth, D. McKissock, A 1 cm space debris impact onto the Sentinel-1A solar array, Acta Astronaut. 137 (2017) 434–443, http://dx.doi.org/10.1016/j.actaastro.2017.05.010.
[6] N. Johnson, Orbital debris: The growing threat to space operations, Adv. Astronaut. Sci. 137 (2010) 3–11.
[7] E.J. Öpik, Collision probabilities with the planets and the distribution of interplanetary matter, Proc. R. Ir. Acad. 54 (1951) 165–199, URL http://www.jstor.org/stable/20488532.
[8] G.W. Wetherill, Collisions in the asteroid belt, J. Geophys. Res. (1896-1977) 72 (9) (1967) 2429–2444, http://dx.doi.org/10.1029/JZ072i009p02429, URL https://agupubs.onlinelibrary.wiley.com/doi/abs/10.1029/JZ072i009p02429.
[9] D. Kessler, B.G. Cour-Palais, Collision frequency of artificial satellites: The creation of a debris belt, J. Geophys. Res. Space Phys. 83 (1978) 2637–2646, http://dx.doi.org/10.1029/JA083iA06p02637, URL https://agupubs.onlinelibrary.wiley.com/doi/abs/10.1029/JA083iA06p02637.
[10] D. Kessler, Derivation of the collision probability between orbiting objects: the lifetimes of Jupiter's outer moons, Icarus 48 (1981) 39–48, http://dx.doi.org/10.1016/0019-1035(81)90151-2.
[11] A. Rossi, L. Anselmo, C. Pardini, R. Jehn, G. Valsecchi, The new space debris mitigation (SDM 4.0) long term evolution code, in: Proceedings of the Fifth European Conference on Space Debris, 2009.
[12] A. Rossi, A. Cordelli, C. Pardini, Modelling the space debris evolution: Two new computer codes, Adv. Astronaut. Sci. Space Flight Mech. (1995).
[13] A. Rossi, L. Anselmo, A. Cordelli, P. Farinella, C. Pardini, Modelling the evolution of the space debris population, Planet. Space Sci. 46 (1998) 1583–1596, http://dx.doi.org/10.1016/S0032-0633(98)00070-1.
[14] H.G. Lewis, G. Swinerd, N. Williams, G. Gittins, DAMAGE: a dedicated GEO debris model framework, in: Proceedings of the Third European Conference on Space Debris, vol. 473, 2001, pp. 373–378.
[15] J. Liou, LEGEND – a three-dimensional LEO-to-GEO debris evolutionary model, Adv. Space Res. 34 (2004) 981–986, http://dx.doi.org/10.1016/J.ASR.2003.02.027.
[16] B. Bastida Virgili, DELTA debris environment long-term analysis, in: Proceedings of the 6th International Conference on Astrodynamics Tools and Techniques, ICATT, 2016.
[17] J. Liou, Collision activities in the future orbital debris environment, Adv. Space Res. 38 (2006) 2102–2106, http://dx.doi.org/10.1016/J.ASR.2005.06.021.
[18] C.R. McInnes, An analytical model for the catastrophic production of orbital debris, ESA J. 17 (1993) 293–305.
[19] F. Letizia, C. Colombo, H.G. Lewis, Analytical model for the propagation of small-debris-object clouds after fragmentations, J. Guid. Control Dyn. 38 (2015) 1478–1491, http://dx.doi.org/10.2514/1.G000695.
[20] F. Letizia, C. Colombo, H.G. Lewis, Collision probability due to space debris clouds through a continuum approach, J. Guid. Control Dyn. 39 (10) (2016) 2240–2249, http://dx.doi.org/10.2514/1.G001382.
[21] D.S. McKnight, F.R. Di Pentino, New insights on the orbital debris collision hazard at GEO, Acta Astronaut. 85 (2013) 73–82, http://dx.doi.org/10.1016/J.ACTAASTRO.2012.12.006.
[22] S. Frey, C. Colombo, S. Lemmens, Extension of the King-Hele orbit contraction method for accurate, semi-analytical propagation of non-circular orbits, Adv. Space Res. 64 (2019) 1–17, http://dx.doi.org/10.1016/j.asr.2019.03.016.
[23] S. Frey, C. Colombo, Transformation of satellite breakup distribution for probabilistic orbital collision hazard analysis, J. Guid. Control Dyn. 44 (2021) 88–105, http://dx.doi.org/10.2514/1.G004939.
[24] L. Giudici, M. Trisolini, C. Colombo, Probabilistic multi-dimensional debris cloud propagation subject to non-linear dynamics, Adv. Space Res. 72 (2) (2023) 129–151, http://dx.doi.org/10.1016/j.asr.2023.04.030, URL https://www.sciencedirect.com/science/article/pii/S0273117723003083.
[25] N.L. Johnson, P. Krisko, J.-C. Liou, P. Anz-Meador, NASA's new breakup model of evolve 4.0, Adv. Space Res. 28 (2001) 1377–1384, http://dx.doi.org/10.1016/S0273-1177(01)00423-9.
[26] J.L. Devore, N.B. Kenneth, Modern Mathematical Statistics with Applications, second ed., Springer New York, 2017, http://dx.doi.org/10.1007/978-1-4614-0391-3.
[27] N. Smirnov, A. Nazarenko, A. Kiselev, Modelling of the space debris evolution based on continua mechanics, vol. 473, European Space Agency, (Special Publication) ESA SP, 2001, pp. 391–396.
[28] F. Jhon, J.P. LaSalle, L. Sirovich, Partial Differential Equations, fourth ed., Springer, New York, 1981.
[29] C. Colombo, Planetary orbital dynamics (PlanODyn) suite for long term propagation in perturbed environment, in: Proceedings of the 6th International Conference on Astrodynamics Tools and Techniques, 2016.
[30] L. Giudici, M. Trisolini, C. Colombo, Phase space description of the debris cloud dynamics through a continuum approach, in: Proceedings of the 73rd International Astronautical Congress, 2022.
[31] D. McKnight, A phased approach to collision hazard analysis, Adv. Space Res. 10 (1990) 385–388, http://dx.doi.org/10.1016/0273-1177(90)90374-9.
[32] V.A. Chobotov, Orbital Mechanics, third ed., AIAA Reston, 2002, http://dx.doi.org/10.2514/4.862250.
[33] O. Montenbruck, E. Gill, Satellite Orbits: Models, Methods and Applications, first ed., Springer Berlin, Heidelberg, 2000, http://dx.doi.org/10.1007/978-3-642-58351-3.
[34] P. Byrd, M. Friedman, Handbook of Elliptic Integrals for Engineers and Scientists, second ed., Springer Berlin, Heidelberg, 1971, http://dx.doi.org/10.1007/978-3-642-65138-0.
[35] J. Loxton, Special values of the dilogarithm function, Acta Arith. 43 (2) (1984) 155–166, http://dx.doi.org/10.4064/aa-43-2-155-166.
[36] D. McKnight, R. Witner, F. Letizia, S. Lemmens, L. Anselmo, C. Pardini, A. Rossi, C. Kunstadter, S. Kawamoto, V. Aslanov, J.-C. Dolado Perez, V. Ruch, H. Lewis, M. Nicolls, L. Jing, D. Shen, W. Dongfang, A. Baranov, D. Grishko, Identifying the 50 statistically-most-concerning derelict objects in LEO, Acta Astronaut. 181 (2021) 282–291, http://dx.doi.org/10.1016/J.ACTAASTRO.2021.01.021.

[37] A. Tan, R.C. Reynolds, M. Schamschula, NOAA-16 satellite fragmentation in orbit: Genesis of the Gabbard diagram and estimation of the intensity of breakup, Adv. Aerosp. Sci. Appl. 7 (2017) 37–47, URL http://www.ripublication.com.

[38] P.D. Anz-Meador, J.N. Opiela, D. Shoots, J.-C. Liou, History of On-Orbit Satellite Fragmentations 15th Edition Orbital Debris Program Office, Tech. rep., 2018, URL http://www.sti.nasa.gov.

[39] P.H. Krisko, Proper implementation of the 1998 NASA breakup model, Orbital Debris Q. News 15 (2011) 4–5.

[40] F. Letizia, C. Colombo, H. Lewis, H. Krag, Development of a debris index, Astrophys. Space Sci. Proc. (2018) 191–206, http://dx.doi.org/10.1007/978-3-319-69956-1.